Exploring MXenes and their MAX phase precursors by electron microscopy

H. Alnoor [a], A. Elsukova [a], J. Palisaitis [a], I. Persson [a], E.N. Tseng [a], J. Lu, L. Hultman, P.O.Å. Persson[*]

Thin Film Physics Division, Department of Physics Chemistry and Biology (IFM), Linköping University, SE-581 83, Linköping, Sweden

ARTICLE INFO

ABSTRACT

This review celebrates the width and depth of electron microscopy methods and how these have enabled massive research efforts on MXenes. MXenes constitute a powerful recent addition to 2-dimensional materials, derived from their parent family of nanolaminated materials known as MAX phases. Owing to their rich chemistry, MXenes exhibit properties that have revolutionized ranges of applications, including energy storage, electromagnetic interference shielding, water filtering, sensors, and catalysis. Few other methods have been more essential in MXene research and development of corresponding applications, compared with electron microscopy, which enables structural and chemical identification at the atomic scale. In the following, the electron microscopy methods that have been applied to MXene and MAX phase precursor research are presented together with research examples and are discussed with respect to advantages and challenges.

More than a decade after the initial publication on graphene [1], two-dimensional (2D) materials remain a focus of the scientific community due to their unprecedented electronic, mechanical, optical, magnetic, and catalytic properties that result from the reduced dimensionality [2]. Among all available 2D materials, the large family of MXenes constitute one of the most rapidly expanding research fields [3].

MXenes are layered transition metal carbides, carbonitrides, and nitrides that were discovered in 2011 [4]. MXenes are produced from layered ternary materials known as the $M_{n+1}AX_n$, or MAX phases, which, in turn, are a large group of layered hexagonal compounds, where M is an early transition metal, A is an A-group element (mostly groups 13 and 14), X is C and/or N and n is 1−3. The layered structure is such that slabs of $M_{n+1}X_n$ are separated by an atomically thin layer of the A element, mostly Al. The prevailing method to form MXene is by selective etching of the A-layers in a MAX phase, to free the corresponding $M_{n+1}X_n$ sheets. The dominant method involves using hydrofluoric acid, HF, or fluoride salts and hydrochloric acid, HCl [5]. Other means of removing the A-layers have been developed including the use of molten salts to

sequentially replace the A-element [6]. When the A-layers are removed, the $M_{n+1}X_n$ sheet surfaces are occupied by terminating species originating from the etchant, including, e.g., O, (OH) and F [7] resulting in weakly bound stacks of 2D sheets with a $M_{n+1}X_nT_x$ composition, where T_x identifies the surface termination [8], which extensively affect the material properties [9] and can be tailored through the choice of etchant [5], molten salt [10], or from gas exposures [11].

In the development of MXenes, two characterization tools have beyond others played an instrumental role in the progression of MXene research. These are X-ray photoelectron spectroscopy (XPS) [12] and electron microscopy. XPS is an attractive analytical technique which is used to investigate the surface chemistry with exceptional detail. The high surface sensitivity of XPS makes it a critical tool in 2D material research. However, the spatial resolution is limited to the square micrometer range. XPS is therefore spatially insensitive, meaning that for powder materials, the signal is compromised by impurities and secondary phases.

In contrast, exceptional spatial resolution is one of the major strengths of electron microscopy, which has served as an essential tool in materials science for nearly a century. In the electron microscope, areas of interest can be identified, selected and investigated by the operator with a spatial resolution below 1 nm in a scanning electron microscope (SEM) and below 1 Å in a (scanning) transmission electron microscope (S)TEM (see Fig. 1 for example).

Fig. 1. Electron microscopes. The double corrected, monochromated, high brightness Linköping Titan[3] 60−300 scanning transmission electron microscope has been extensively for the studies of layered MAX phases and 2D MXenes. Capable of spatial resolution ~70 pm and ~70 meV energy resolution, many similar instruments are installed worldwide and involved in corresponding research.

Moreover, modern electron microscopes are capable of simultaneously providing data about morphology, crystal structure and atomic arrangement, elemental composition, and chemical state. Currently, it is the only technique, which allows to comprehensively study 2D materials at the atomic level. Recent developments of environmental instruments and sample holders allow for *in situ* investigations on dynamic changes of materials that can be executed in controlled gas or liquid environments. Essentially, this allows researchers to move the lab inside the electron microscope by miniaturizing the experiments. These investigations are particularly relevant for the fundamental understanding and for further optimizing the electrochemical or catalytic performance of the material.

In this review, we summarize the contribution of electron microscopy investigations in MXene and MAX phase precursor research. The emphasis is on the achievable materials science because extensive textbooks are available on the technology. However, with increasing complexity and degree of

Fig. 2. Front cover SEM images of MXenes. Ti_3C_2 featured on (a) Advanced Materials and (b) Nanotoday. Fig (a) adapted with permission from a study by Naguib et al. [4], Copyright (2011) WILEY-VCH Verlag GmbH & co. KGaA and Fig (b) adapted with permission from author (B. Anasori). SEM, scanning electron microscope.

information, we discuss the available methods and their limitations, as well as finally suggest future research directions.

Fundamental to all materials research, the SEM constitutes a characterization method that is easily accessible also for the novice. In connection with MXenes and their MAX phase precursors, the SEM is potentially the one instrument that has contributed beyond others to the success and rise of MXenes research by generates high resolution images over 5 orders of magnitude in magnification by rastering an electron beam across a sample. Back-scattered electrons or secondary electrons provide information on the topography, morphology, and microstructure, while generated X-rays provide compositional information and elemental maps. For more information on the beam-material interactions, please consult a textbook on SEM (e.g. L. Reimer [14]). SEM images are easily interpreted and generate high impact images that immediately convey the potential of this material. Accordingly, striking MXene SEM images have frequently been on the cover of high impact factors journals [4,15,16]. This includes Fig. 2 (a) which shows a colored view SEM image which featured on the front cover of Advanced Materials, that reported on the first synthesized MXene $(Ti_3C_2T_x)$ by Naguib et al. [4]. A similarly striking cover is that from B. Anasori et al. [13] in Fig. 2(b).

Generally, SEM imaging of MXenes, is used to confirm the morphology and the conversion process, starting from the bulk MAX phases and eventually the 2D MXenes structure [4,17−20]. Because the MAX and MXene powders are predominantly analyzed after processing, the information is static. As an example, Fig. 3 shows overview SEM images combined with energy-dispersive X-ray (EDX) analyses (insets) that reveals the layered structure of MAX phase (V_4AlC_3) and to verify the successful removal of the Al layer, yielding the morphology of multilayered 2D MXene $(V_4C_3T_x)$ [17].

SEM imaging is also used to understand or verify the success of other processing routes, by gaining insight in the morphological changes from MAX bulk to MXene sheets/flakes by using, e.g., wet chemical methods or heating, to study or enhance the MXene properties, which is desirable for many applications [21−26]. Fig. 4 provides examples of post-processing morphologies of MXenes, where Fig. 4(a) displays a top-view SEM image showing the assembly of Ti_3C_2 nanosheets to 3D architectures where MXene sheets assume crumpled shapes with numerous ridges and rough
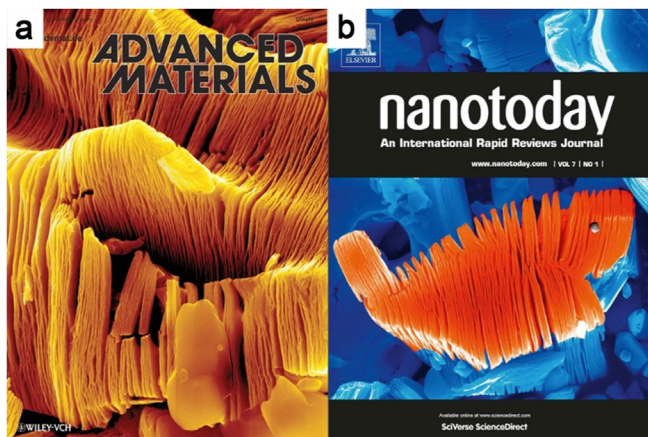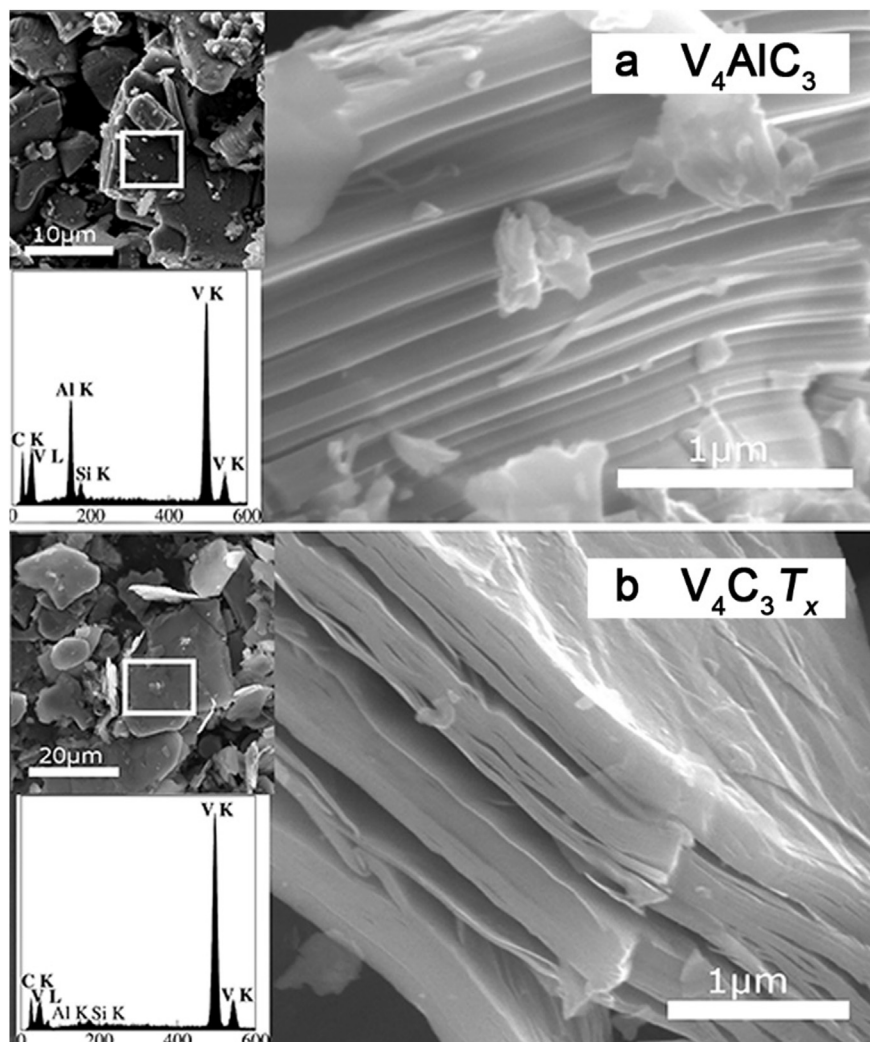
Fig. 3. SEM imaging and EDX of MAX/MXenes. (a) V_4AlC_3 (MAX phase) and (b) $V_4C_3T_x$ (MXene). Insets shows EDX analyses, the white boxes indicating where the EDX analyses were performed. Adapted with permission from a study by Tran et al. [17]. Copyright (2018) American Chemical Society. SEM, scanning electron microscope; EDX, energy-dispersive X-ray.

surface upon using a capillary-forced assembling strategy [21]. While in Fig. 4 (b), SEM image is used to demonstrate the wrinkled morphology of $Ti_3C_2T_x$ flakes that were treated with NaOH [22]. SEM imaging performed in a cross-sectional mode of vacuum-assisted filtrated MXene suspensions or composites is typically applied as a quick and trustworthy method to quantify the film thickness, which is essential knowledge to quantify electrochemical properties [27–29]. Examples of this are Fig. 4(c–d), which show cross-sectional SEM images that reveal an ordered, compact, and layered $Ti_3C_2T_x$ film [27], as well as the porosity features of a $Ti_3C_2T_x$/CNT composite [29].

In contrast, the TEM is a more complex instrument than the SEM and a number of extensive textbooks are available [30]. The TEM requires extensive operator training and many times also extensive sample preparation. Immediate benefits include imaging magnifications across five orders of magnitude and a spatial resolution well beyond the lattice structure, which is essential for the investigation of 2D materials. TEM images are achieved by transmitting a highly coherent electron beam through the sample and detecting the scattered electrons. A sample image is formed in the image plane of an electromagnetic objective lens and eventually captured by a CCD camera. Because the electron beam passes through the sample, the

thickness is a critical component as too much material degrades the image quality. In 2D material research, this is not a concern in most cases.

Coherent TEM imaging provides a more detailed microstructure characterization, compared with the SEM, allowing detection of immediate contrast differences between phases, crystal orientations, and conducting statistical analysis of flakes' size and dimensions [17,32–34]. Furthermore, the observation of lattice fringes in high resolution images provides interpretable information on the structure, including lattice spacing and orientation relations [4,31,35–40].

The TEM investigation of MAX phases were performed long before MXenes were discovered and Fig. 5(a), shows an example of a low-magnification TEM image exhibiting characteristic differences within the microstructure present in the as-synthesized Ti_3AlC_2 MAX ceramic, including grains with different orientation as well at the presence of competing phases (Al_3Ti). Extensive TEM observations of MAX phases reveal characteristic features, including the layered zig-zag appearance, that are remarkably different from competing phases such as the tetragonal Al_3Ti. From the lattice resolved image in Fig. 5(b), the Zr_3AlC_2 reveals the apparent layering along the [0001] crystallographic direction [32].
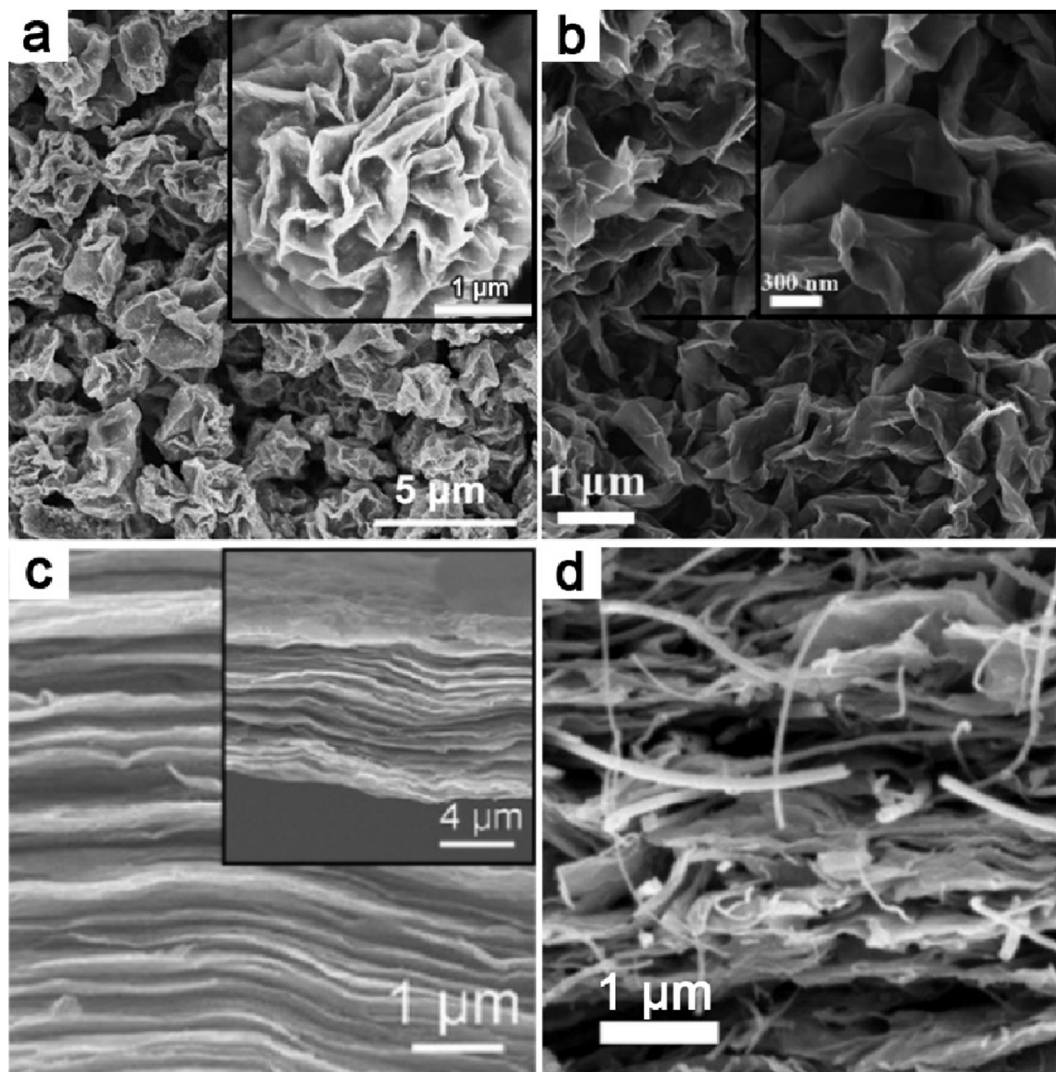
Fig. 4. Top-view and cross-sectional SEM imaging of MXenes. (a) Three dimensional architectures $Ti_3C_2T_x$ with fluffy shape. (b) Crumpled Na-c-$Ti_3C_2T_x$. (c) $Ti_3C_2T_x$ film. (d) Porous $Ti_3C_2T_x$/carbon nanotube composite. Insets show higher magnified images in (a) and (b) and lower magnified image in (c). Scale bars in (d) correspond to 1 μm. Adapted with permission from [21,22,27,29], respectively. Copyright (2018) The Royal Society of Chemistry, Copyright (2018) American Chemical Society, Copyright (2017) WILEY-VCH Verlag GmbH & co. KGaA, Copyright (2016) Elsevier, respectively. SEM, scanning electron microscope.

It is tempting to relate the apparent dotted appearance of the high-resolution TEM (HRTEM) image to the atomic structure. However, this approach requires extensive control of the imaging conditions, best supported by image simulations and is not immediately straightforward. High-resolution lattice-resolved images should therefore be considered as representative for the periodicity of the crystalline structure and can provide crystallographic relations, as well as identification of crystalline spacings.

One particular strength of TEM is the accessibility of reciprocal space information through the switch of a button, which enables acquisition of electron diffraction (ED) from the same area illuminated and observed in the image mode. This is carried out by focusing the diffraction (back focal) plane instead of the image one on CCD. Similar to X-ray diffraction, ED is applied for the interpretation of crystal structures [18,31,33,35,37,41−45] and phase identification of small crystals. ED patterns (EDPs) can be obtained from nanoscale crystals that are selected within a diffraction aperture (selected area electron diffraction [SAED]) or by a focused electron beam (convergent beam electron diffraction [CBED]) [46].

As an example, Fig. 5(c−e) are SAED of hexagonal Ti_3AlC_2, which are indexed as [0001], [$1\bar{2}10$], and [$1\bar{1}00$] low-index basic zone axes, respectively. Accurate lattice parameters can be derived against a reference or by a well calibrated microscope. These EDPs are also informative for determining the extinction rules. In the [$1\bar{2}10$] EDP, all reflections appear, but in [$1\bar{1}00$], the ($000l$) reflections with $l =$ odd are extinct, implying the existence of a c glide plane. Fig. 5(f) shows an EDP, the orientation of which is positioned between [$1\bar{2}10$] and [$1\bar{1}00$]. It can be seen from Fig. 5 (f) that the (000l) reflections with $l =$ odd are also extinct, which indicates that there is a 6_3 screw axis along the [0001] axis. Similarly, the CBED pattern in Fig. 5(g) shows the symmetry of a six-fold rotation about the [0001] axis and also the symmetry of a mirror reflection across the ($1\bar{2}10$) and ($10\bar{1}0$) planes. Fig. 5(h) shows the CBED pattern evidencing the existence of a mirror plane on (0001). A combination of information derived from EDPs, and the CBED patterns indicates that Ti_3AlC_2 has a point group of 6/mmm and a space group of $P6_3$/mmc [31], as well as demonstrates the use of ED in structure determination.
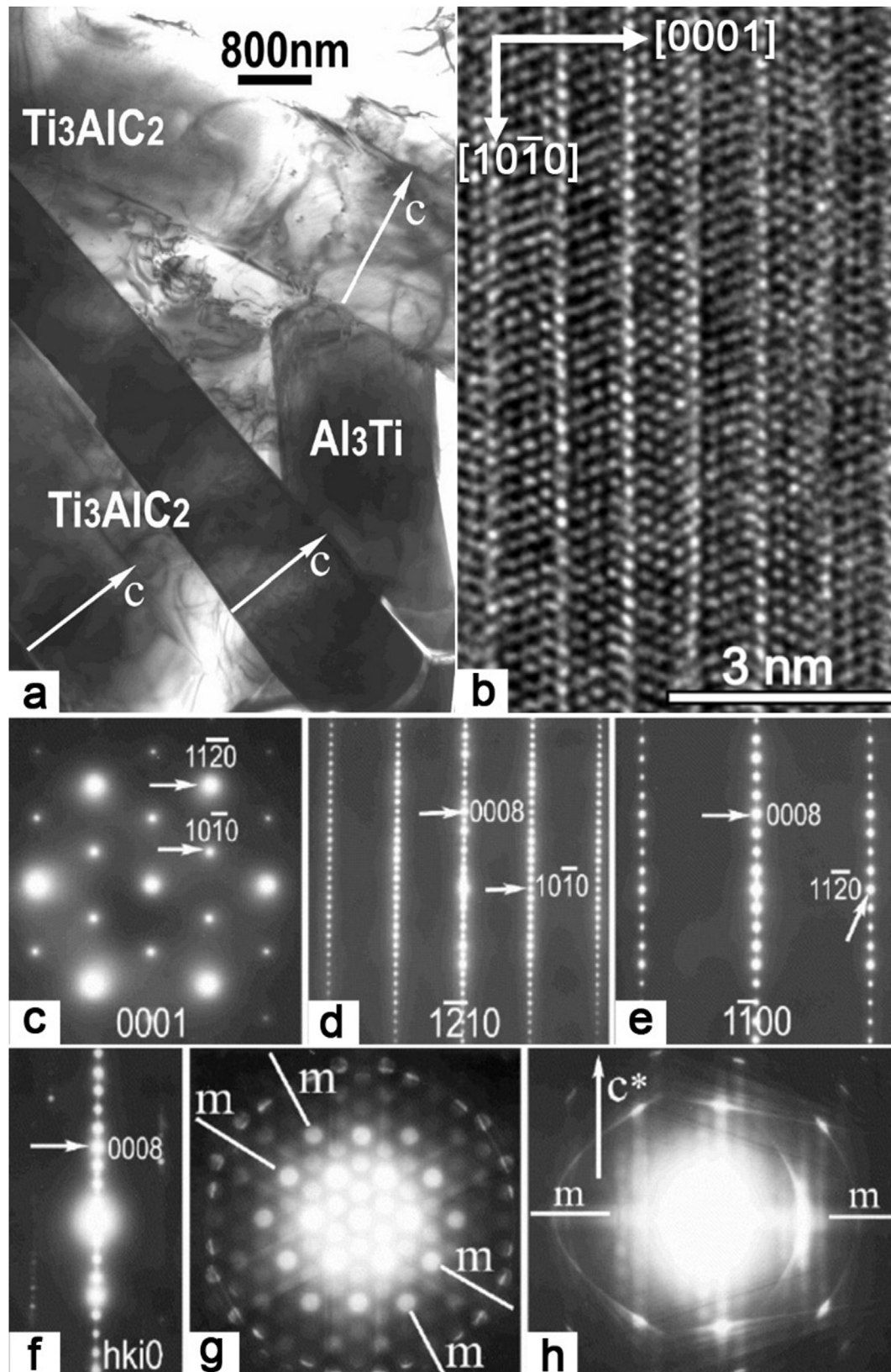
Fig. 5. TEM imaging and SAED of MAX phases. (a) TEM image of polycrystalline Ti$_3$AlC$_2$ MAX phases [31]. (b) HRTEM image of Zr$_3$AlC$_2$ taken with the incident beam parallel to the [11$\bar{2}$0] direction [32]. Adapted with permission from a study by Lapauw [32]. Copyright (2016) European Ceramic Society. SAED patterns of Ti$_3$AlC$_2$ acquired along (c) [0001], (d) [1$\bar{2}$10], and (e) [1$\bar{1}$00]. (f) A SAED of the orientation of which is positioned between [1$\bar{2}$10] and [1$\bar{1}$00]. (g) CBED showing the symmetry of a six-fold rotation about [0001] axis and also the symmetry of mirror reflection across the (1$\bar{2}$10) and (10$\bar{1}$0) planes. (h) A CBED pattern showing the existence of a mirror plane on (0001) [31]. Adapted with permission from a study by Ma et al. [31]. Copyright (2004) Philosophical Magazine. TEM, transmission electron microscope; HRTEM, high-resolution TEM; SAED, selected area electron diffraction; CBED, convergent beam electron diffraction.
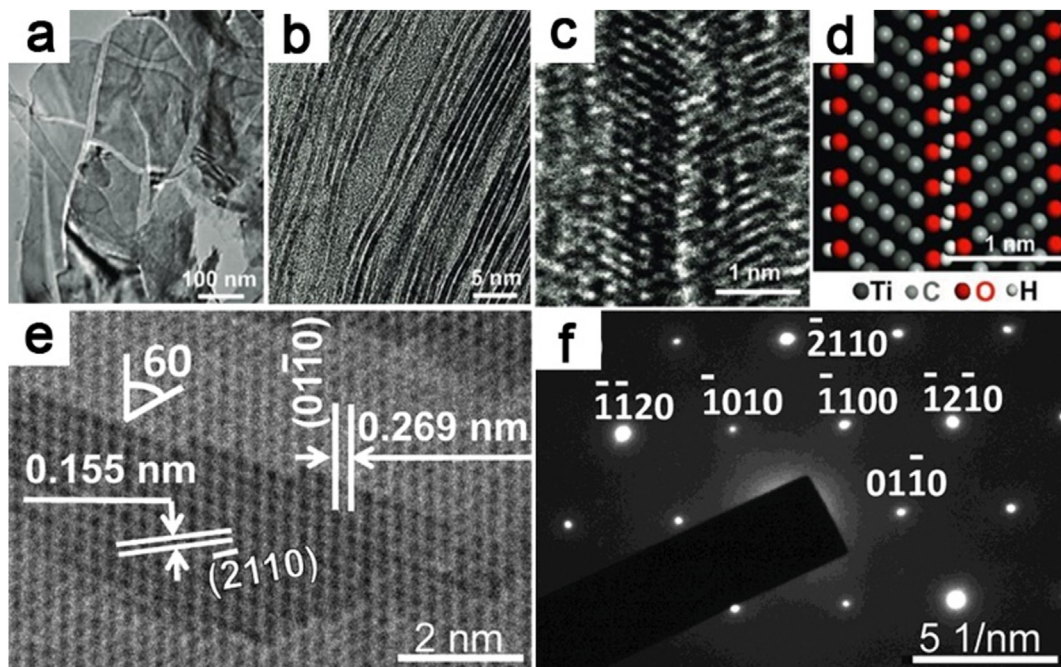
Fig. 6. TEM imaging and SAED of MXenes. (a) TEM image of exfoliated 2D nanosheets of Ti-C-O-F. (b) Single and double layer MXenes sheets. (c) HRTEM image of bilayer $Ti_3C_2(OH)_xF_y$ and (d) its atomistic model of the layer structure [4]. Adapted with permission from a study by Naguib et al. [4]. Copyright (2011) Advanced Materials. (e) HRTEM image of multilayer MXene with (f) SAED pattern [18]. Adapted with permission from a study by Naguib et al. [18]. Copyright (2012) American Chemical Society. TEM, transmission electron microscope; SAED, selected area electron diffraction; HRTEM, high resolution TEM.

Imaging and diffraction of 2D materials such as MXenes are in general more easily interpreted compared with 3D particles, owing to strong reduction of dynamic effects (multiple scattering of the electron beam). Plan-view TEM imaging of exfoliated MXene sheets, Fig. 6(a) reveals typical uniform-contrast sheets that

strongly suggests a very thin foil. Low-magnification TEM images similar to the one in Fig. 5(a) allow access to information about MXene sheet size and structural integrity after etching. In this case, Fig. 6(b) shows a cross-sectional image from layers of exfoliated single- and double-layer MXene sheets, from which the degree of
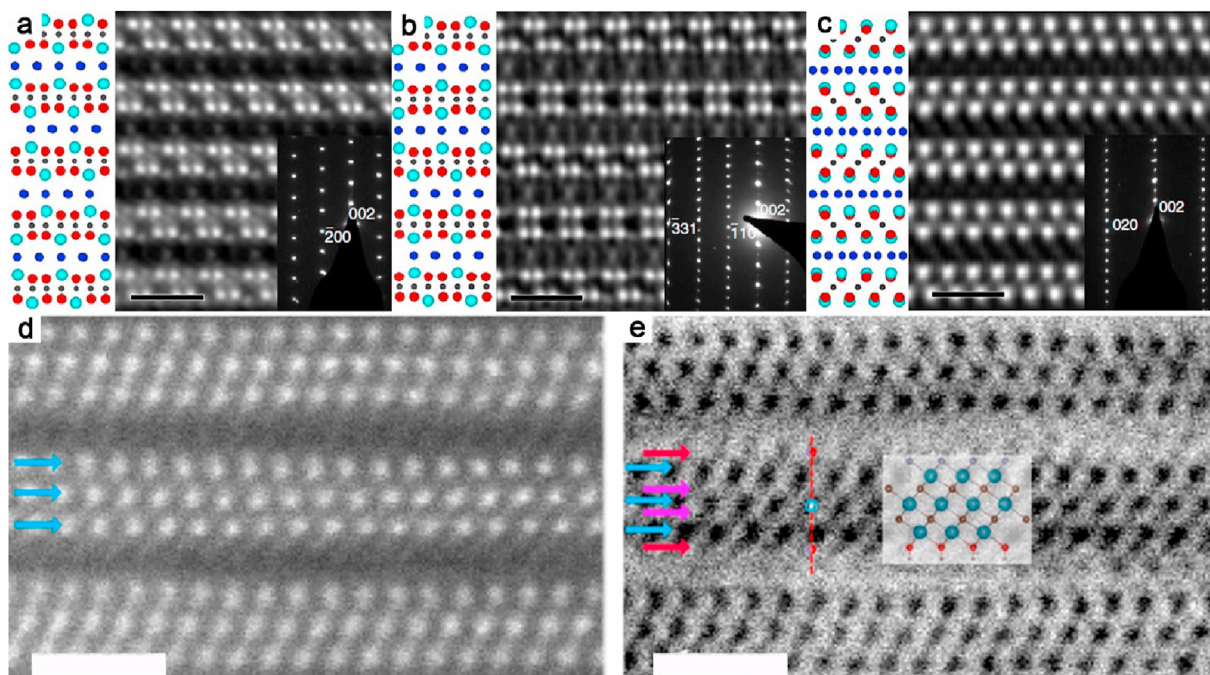

Fig. 7. Cross-sectional STEM imaging of MAX/MXenes. (a–c) In-plane chemical ordered $(Mo_{2/3}Sc_{1/3})_2AlC$ i-MAX imaged by HAADF along the (a) [010], (b) [110], and (c) [100] zone axis with corresponding SAED patterns and atomic model arrangements. Adapted from a study by Tao et al. [52]. Copyright (2017) Springer Nature under Creative Commons CC BY license. (d–e) Multilayer Ti_3C_2X MXene resolved by combined (d) HAADF and (e) ABF. Adapted with permission from a study by Wang et al. [66]. Copyright (2015) American Chemical Society. Scale bars in (a–e) correspond to 1 nm. STEM, scanning transmission electron microscopy; SAED, selected area electron diffraction; HAADF, high-angular annular dark-field; ABF, annular bright-field.
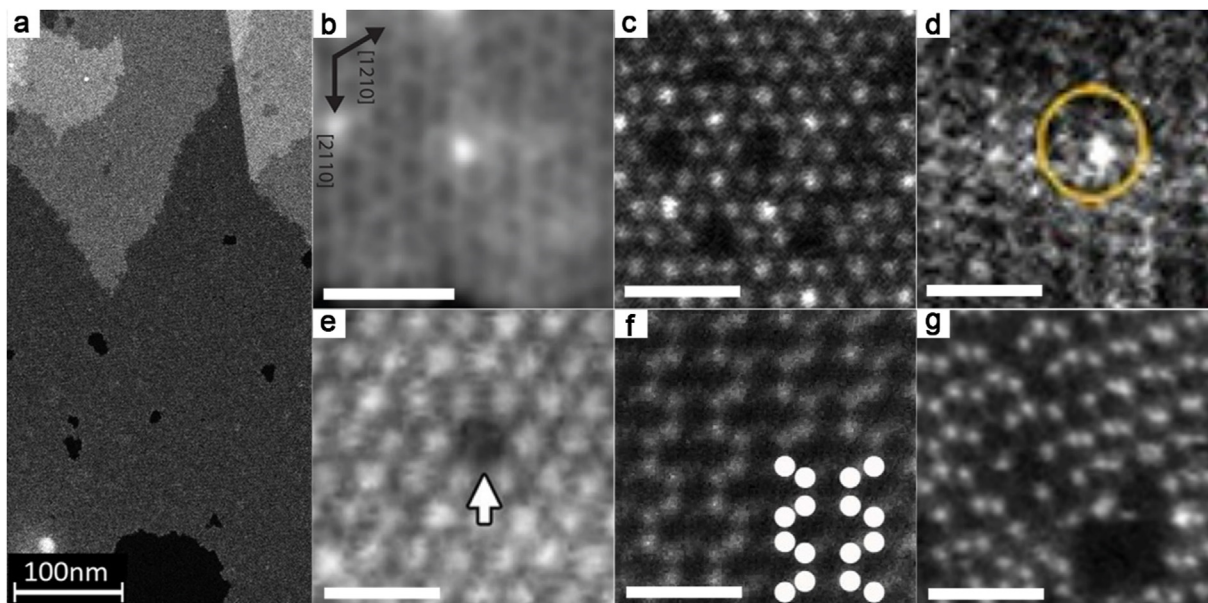
Fig. 8. Plan-view STEM imaging of MXenes. (a) Overview HAADF image from $V_{2-x}C$ MXene. Adapted from Thörnberg et al. [51]. Copyright (2019) The Royal Society of Chemistry 2018 under Creative Commons Attribution 3.0 Unported License. HAADF images of defects in single-layer MXene sheets revealing (b) Ti adatom on Ti_3C_2. Adapted with permission from a study by Karlsson et al. [68]. Copyright (2015) American Chemical Society. (c) Multiple Nb adatoms on Nb_2CT_x. Adapted from a study by Palisaitis et al. [69]. Copyright (2018) The Royal Society of Chemistry 2018 under Creative Commons Attribution 3.0 Unported License. (d) Isolated Pt atom on $Ti_{3-x}C_2T_y$. Adapted with permission from a study by Zhao et al. [70]. Copyright (2019) American Chemical Society. (e) Ti vacancy in Ti_3C_2. Adapted with permission from Sang et al. [71]. Copyright (2016) American Chemical Society. (f) Divacancies in $Mo_{1.33}C$. Adapted from a study by Tao et al. [52]. Copyright (2017) Springer Nature under Creative Commons CC BY license. (g) random vacancies in $Nb_{1.33}CT_x$. Adapted with permission from a study by Halim et al. [54]. Copyright (2018) American Chemical Society. Scale bars in (b–h) correspond to 0.5 nm. STEM, scanning transmission electron microscopy; HAADF, high-angular annular dark-field.

separation between sheets, as well as the average separation, can be identified. Fig. 6(c) and (d) show the cross-section HRTEM image and suggested atomistic model of two adjacent terminated Ti_3C_2 sheets, respectively [4]. In general, any direct comparison between real and potential structures, requires extensive simulations and experimental control. Other comparisons can only be qualitative.

Plan-view HRTEM and SAED in Fig. 5(e) and (f) demonstrate that the crystallinity of the $M_{n+1}X_n$ sheets from the MAX phases is retained during etching and exfoliation. The images in Fig. 6(e) and (f) exemplify the preserved hexagonal structure of Ti_4C_3 MXene, where measurements of d-spacings are directly obtained for the $(01\bar{1}0)$ and $(\bar{2}110)$ lattice planes, respectively. The lattice parameter $a = 0.31$ nm calculated from these values matches the parent Ti_4AlC_3 MAX phase (0.311 nm) [18]. Typically, such measurements must be undertaken with care. The microscope must be calibrated from a known reference sample, typically gold nanoparticles or film. In case of SAED, one has to set parallel illumination conditions and make sure that diffraction plane is properly focused on CCD camera. Typically, the d-spacings are calculated using SAED pattern. However, when the crystal size is smaller than the smallest available selected area aperture the SAED may be difficult to interpret. In this case the d-spacings can be determined by obtaining first the HRTEM image and then applying the Fast Fourier transform to the region of interest, as these provide equivalent information albeit at a lower resolution, which must be taken into account when estimating the error bar.

While the interpretation of TEM images suffer from the highly coherent nature of the electron beam, scanning transmission electron microscopy (STEM) is regarded as one of the most powerful techniques for visualizing the crystal structure and enables observation of materials with elemental-dependent contrast on the atomic scale. At present, it is the dominant method in the field for direct identification and understanding of MAX phase and MXene atomic structures. In STEM, a subatomic-sized beam is rastered across the sample and the forward scattered electrons are detected by an annular dark-field detector. Depending on collection angle different type of images can be obtained. For high angles (80−200 mrad), so-called high-angular annular dark-field (HAADF) images are formed. HAADF image contrast is commonly referred to as directly interpretable elemental contrast due to its strong dependence on atomic number and scales with $\sim Z^{1.64}$ and thickness (Z-atomic number) [47]. For 2D materials, the thickness increases at integer values (number of sheets) and can be ignored to a first approximation for a single 2D sheet; hence, the contrast is directly related to the atomic mass. The weakness of the method constitutes weak scattering and associated signal from the lighter X and T_x elements, e.g., C, O, and F that are relevant for MXene research, making them indistinguishable in the HAADF next to the heavier M elements (e.g., Ti and Mo), which can be rather accurately differentiated.

MAX phases and multilayer MXenes are commonly investigated from cross-section projections (perpendicular to c-axis), which enables identification of elemental stacking in MAX phases, separation between MXene sheets, stacking of sheets, and ordering of terminating surface group (for multilayer (ML)-MXene). Plan-view investigations are ideally suited for a single sheet MXene, revealing the atomic structure, surface functionalization, arrangements of point defects and their clusters.

Cross-sectional high-resolution HAADF imaging is a powerful method for crystals structure determination by observing the atomic structure of MAX phases from different projections. This has enabled the identification of a range of novel multiM MAX phases with out-of-plane (o-MAX) [48] and in-plane (i-MAX) [49−55] chemical ordering between the M-elements. As an example, HAADF imaging, performed from the primary cross-sectional projections, enabled the identification of the in-plane chemical ordering in novel MAX phases. Fig. 7(a−c) shows HAADF images acquired from the quaternary $(Mo_{2/3}Sc_{1/3})_2AlC$ MAX phase viewed
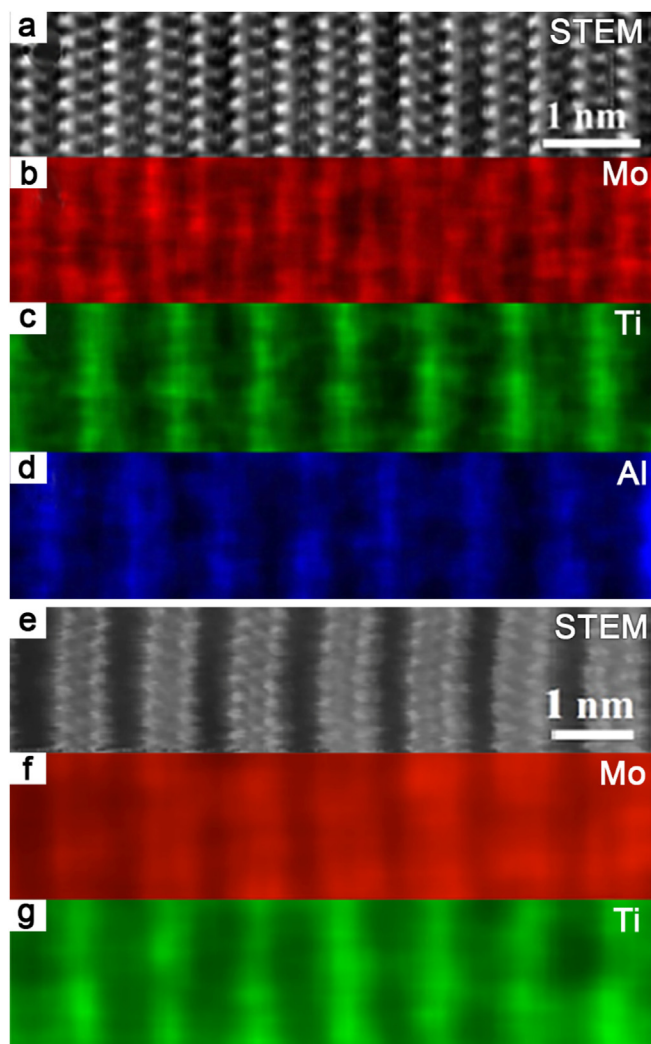
Fig. 9. STEM-EDX mapping of MAX/MXene. (a) HAADF image of Mo_2TiAlC_2 MAX phase with corresponding EDX maps for: (b) Mo, (c) Ti, (d) Al. Adapted from a study by Anasori et al. [48], with the permission of AIP Publishing. (e) STEM image of Mo_2TiC_2 MXene with corresponding EDX maps for: (f) Mo, (g) Ti. Adapted from ra study by Anasori et al. [19], further permissions related to the material excerpted should be directed to the ACS Publications. STEM, scanning transmission electron microscopy; EDX, energy-dispersive X-ray; HAADF, high-angular annular dark-field.

along the [010], [110], and [100] zone axis. In Fig. 7 (c), the structure looks identical to a traditional MAX phase viewed along the [11−20] zone axis [6,54]. However, evidence for in-plane ordering of the two transition metals is revealed in Fig. 7(a) and (b), respectively, where the former image rules out orthorhombic symmetry. The in-plane ordered MAX phase structure was corroborated by selective area ED as shown in the insets of Fig. 7(a−c). These images further verify that a more direct interpretation of the atomic structure is permitted, e.g. the M atomic columns are perfectly in position when compared with the calculated model structures. However, the intensity of the A layer element (Al) is not directly comparable (e.g., every 2nd atomic column vanishes in Fig. 7(a)), which is ascribed to electron channeling for thick specimens [56,57] and can be identified through image simulations [58,59]. The same investigation strategy applies when studying multilayer stacked MXenes [17,60−65].

Using a large convergence angle beam (20−30 mrad) and lower collection angles (10−25 mrad) annular bright-field (ABF) images are obtained. Enhanced sensitivity for light elements, with retained

imaging of heavier elements, can be achieved using ABF imaging as contrast exhibits a $Z^{1/3}$ dependence [67], enabling simultaneous imaging of, e.g, C and Ti.

Both light and heavy elements appear as dark spots and have similar contrast. However, the ABF images become increasingly difficult to interpret with increasing thickness due to its semi-coherent nature. The most comprehensive information about the atomic arrangement of a sample can be obtained by complimentary HAADF and ABF imaging, see Fig. 8(d−e).

This approach was used on multilayer $Ti_3C_2T_x$ MXene [66] and permitted visualization of surface structures and functional groups. Fig. 7(d) shows a cross-sectional HAADF image indicating the skeleton of the $Ti_3C_2T_x$ MXene emphasizing the Ti atomic layers. The light atomic layers (such as C, O, and F) were visualized by ABF imaging as shown in Fig. 7(e).

The atomic structure information obtained from cross-sectional MXene investigations as shown in Fig. 7(d−e) is subject to uncertainty due to projection of an undefined number of atoms (and/or unknown mix of atoms) in the columns. To unambiguously resolve the atomic structure of individual MXene sheets requires studying single MXene sheets in plan-view projection.

Similar for SEM and TEM, overview plan-view HAADF images are typically used to verify the sheet-like nature and morphology of the micrometer size MXene sheets (e.g., flat, scrolls or crumbled), as well as to distinguish the number of layers from the HAADF contrast variations [51,65,72]. Fig. 8 (a) shows an overview HAADF image acquired from V_2CT_x MXene revealing flat morphology and showing macroscopic pores (black contrast) [51]. The sheet exhibits different thicknesses as evidenced from intensity variations in the image (contrast increases with number of layers). The non-overlapped, well orientated (non-bent), single sheet flakes (darkest contrast) must be chosen for the high resolution, atom-by-atom, structural analysis.

Plan-view HAADF approach enables direct imaging of individual point defects in single sheets as shown in Fig. 8(b−g). (b) shows native adatoms (originating from the MAX/MXene) [68], (c) saturation of native adatoms [69], (d) foreign adatoms (not originating from the MAX/MXene) [70,73,74], (e) single vacancies [71], (f) ordered vacancies [50,52−54], and (g) random vacancies [54]. Besides, surface functionalizing groups and their mobility could be visualized using this approach [75].

Imaging in both the SEM and the TEM can be greatly enhanced by chemical analysis and elemental mapping throughout the magnification range via EDX spectroscopy [17,62]. Interaction between a swift electron and an atom may lead to the emission of an element-specific X-ray photon. Combined with high resolution STEM imaging, it enables direct identification of the crystal structure paralleled with determination of the spatial distribution of the elements in the lattice [6,19,48,52,53,76,77]. As an example, Anasori et al. [48] used EDX mapping to prove the formation of the out-of-plane ordered Mo_2TiAlC_2 o-MAX phase and its corresponding Mo_2TiC_2 o-MXene [19]. Fig. 9(a) and (e) show high-resolution STEM image of Mo_2TiAlC_2 and Mo_2TiC_2, respectively, both viewed along the [11−20] zone axis. The corresponding elemental EDX maps Fig. 9(b−d) and (f-g)) reveal that every Ti layer (green) is sandwiched between to Mo layers (red). For the o-MAX phase, the A (Al) layers positioned between M (Mo-Ti-Mo) layers can be also be directly identified (Fig. 9(d)).

Another spectroscopy technique commonly available in the TEM is electron energy loss spectroscopy (EELS) [80]. It is based on detecting the amount of energy the incident electron loses after an inelastic scattering event. While EDX spectroscopic acquisition and analysis are more straightforward, EELS provides a wider range of information about material properties. The EELS spectrum can be roughly divided into two parts: high (or core)- and low-loss energy
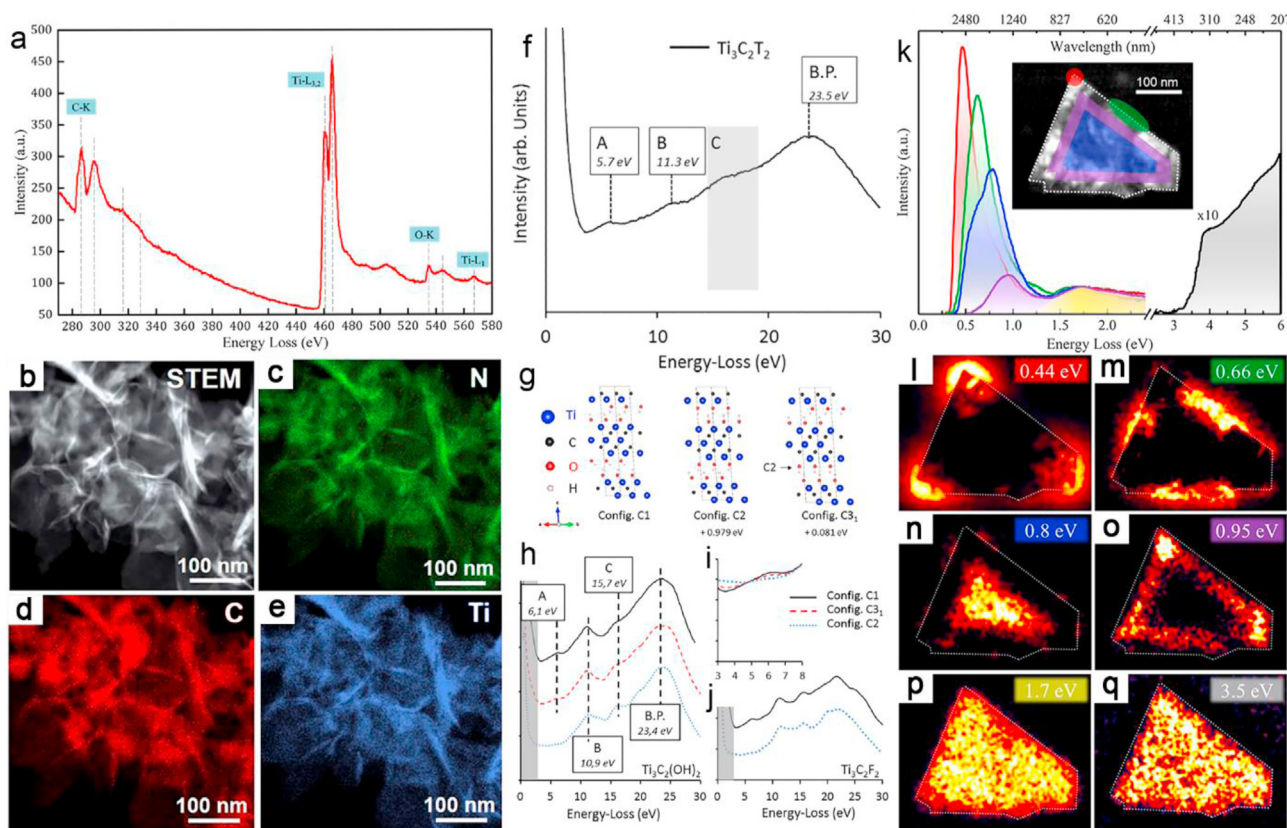
Fig. 10. Chemical mapping by core-loss EELS. (a) Core-loss EELS of Ti₃C₂Tₓ MXene displaying characteristic C-K, Ti-L₃,₂, O-K and Ti-L₁ edges. Adapted with permission from a study by El-Demellawi et al. [81]. Copyright (2018) American Chemical Society. (b) HAADF image and (c-d) corresponding EELS elemental mapping images of nitrogen-doped Ti₃C₂ MXene. Adapted from a study by Song et al. [82]. Copyright (2020) with permission from Elsevier. Identification of surface functionalization sites in the multilayer Ti₃C₂T₂ MXene using the combination of valence electron energy-loss spectroscopy (VEELS) and ab initio calculations. (f) Experimental VEEL spectrum recorded on multilayer Ti₃C₂T₂ MXene. Adapted with permission from a study by Magne et al. [88]. Copyrighted by the American Physical Society. (g) Three surface group configurations considered for the calculations of the theoretical VEEL spectra. (h) Theoretical VEEL spectra calculated for different Ti₃C₂(OH)₂ configurations with (i) enlarged energy range near 6.1 eV. (j) Theoretical VEEL spectra of the C1 and C2 configurations of Ti₃C₂F₂. Adapted with permission from a study by Magne et al. [88]. Copyright (2015) by the American Physical Society. Mapping spatial distribution of surface plasmon modes by low-loss EELS. (k) Low-loss EELS spectrum acquired on a truncated triangular Ti₃C₂Tₓ MXene flake. Zero-loss peaks are subtracted. The spectra are normalized to the peak at 1.7 eV (yellow shading) and magnified by a factor of 10 above 2.5 eV. Inset: HAADF image of the Ti₃C₂Tₓ flake on a Si₃N₄ supporting membrane (black area). Red circle, green ellipse, blue and purple areas mark the positions of the most intense excitation for the dipole, quadrupole, and central modes, respectively. White dotted contour defines the perimeter within which the transversal mode (1.7 eV) and IBT (3.5 eV) could be excited. (l-q) EELS fitted intensity maps of the corresponding SP modes and IBT sustained by the flake at the energy losses plotted in (k). Dotted lines define flake boundaries. Adapted with permission from a study by El-Demellawi et al. [81]. Copyright (2018) American Chemical Society. (For interpretation of the references to color in this figure legend, the reader is referred to the Web version of this article.) HAADF, high-angular annular dark-field; EELS, electron energy loss spectroscopy; SP surface plasmon.

loss regions. The core-loss spectrum (typically 50−1000 eV) contains characteristic features (ionization edges) arising from the electron interaction with the inner shell(s) of the atom. A key advantage of EELS in relation to elemental mapping of MXenes is its efficiency in detecting and quantifying light elements including C, N, O, and F.

An example of the core-loss spectrum obtained from Ti₃C₂Tₓ MXene [81] is presented in Fig. 10(a), where the characteristic C-K, Ti-L₃,₂, O-K, and Ti-L₁ edges can be observed at approximately 283.5, 460.3, 535, and 567 eV, respectively. When combined with STEM mode, EELS can also be used for elemental mapping across the magnification range, down to the atomic scale [17,68,69,82,83]. Song et al. synthesized nitrogen-doped Ti₃C₂Tₓ MXene for application in electrocatalysis and applied STEM-EELS core loss elemental mapping to confirm the presence of N, C, and Ti (Fig. 10(b−e)).

The significance of EELS is its sensitivity to detect local (i.e. spatially resolved) chemical states and environments in a sample. MXenes' materials properties and therefore their capacity in applications strongly depend on the surface termination and their arrangement on the MXene surface. EELS in combination with

STEM provides a local probe to determine the nature and location of these terminations, for which there are two approaches. The first is to remain in the core-loss region and identify the fine structure of characteristic elemental edges, also known as the energy loss near edge structure (ELNES). ELNES signal is produced by transitions of electrons from the inner-shell to unoccupied states and in combination with electronic structure calculations provides information on the local atomic arrangement such as interatomic distances, coordination numbers, symmetry, and electronic structures including valency, spin state, and chemical bonding [84]. A direct interpretation of ELNES is not feasible and requires comparison with computational efforts. This approach was used by Magne et al. who used the fine structure of C-K and F-K edges combined with DFT calculations to study surface functionalization of multilayer Ti₃C₂Tₓ MXenes [85]. Another approach is to move to the low-loss region (<50 eV), also referred to as valence EELS (VEELS), which contains various peaks and features associated with the excitation of the valence electrons of the solid, such as surface plasmons, bulk plasmons (BP), and interband transitions [86,87]. The main advantage of VEELS constitutes its orders of magnitude more intense signal in low-loss region as compared with the core-loss
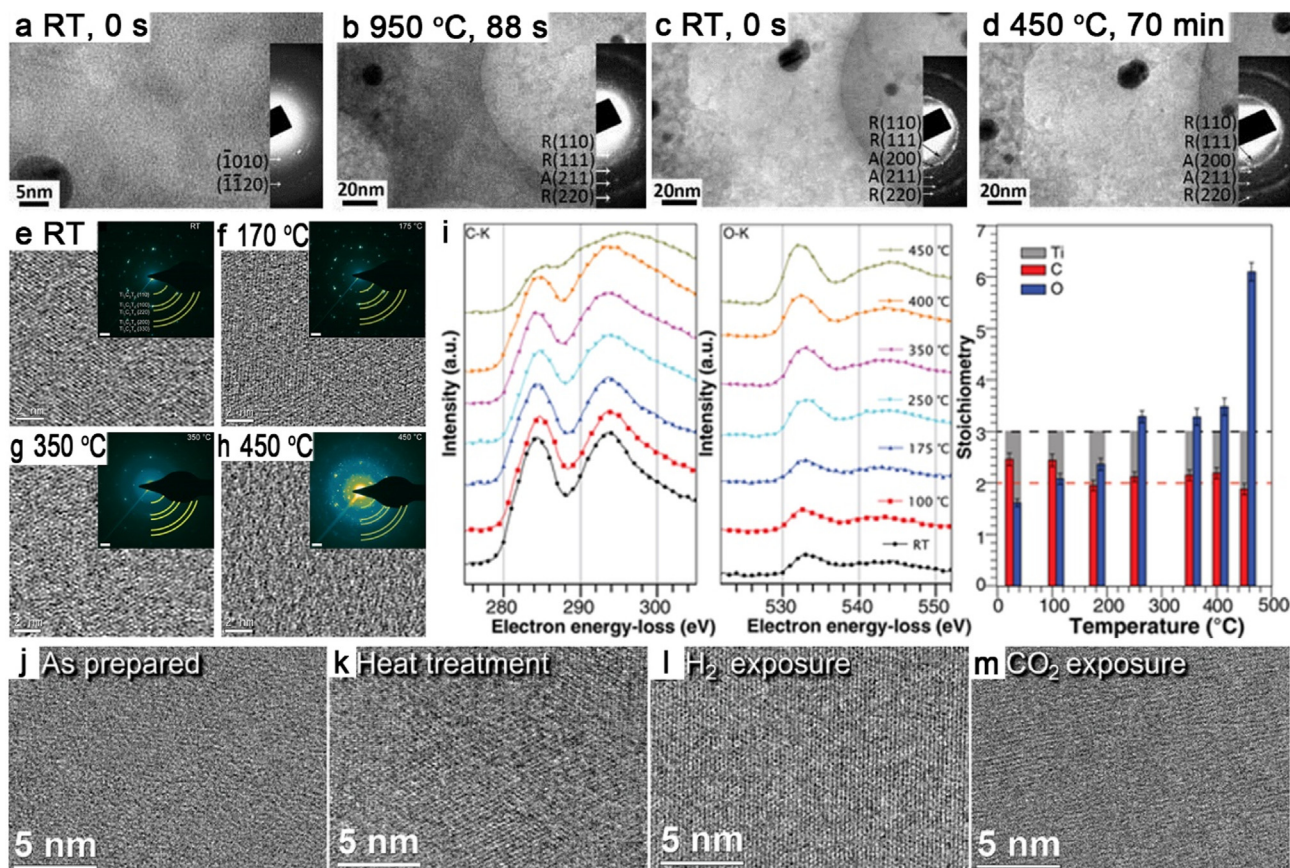
Fig. 11. In situ gas experiments on MXenes: (a–b) TEM images showing oxidation evolution of a Ti_3C_2 MXene multilayer particle during slow heating (over 70 min) in O_2 environment from; (a) RT, (b) 260 °C, (c) 350 °C, and d) 450 °C. ED insets reveal TiO_2 rutile (R) and anatase (A) formation. Adapted with permission from a study by Ghassemi et al. [92]. Copyright (2014) Royal Chemistry of Society. (e-f) Shows HRTEM images of a single flake $Ti_3C_2T_x$ surface as a function of low pressure oxidation at (e) RT, (f) 175 °C, (g) 350 °C, and (h) 450 °C. ED insets evidence the MX structure and TiO_2 particle formation onset at 450 °C. (i) EELS spectra illustrating the evolution of O_x surface coverage with respect to Ti_3C_2 as a function of temperature. Adapted from a study by Persson et al. [93]. Copyright (2020) WILEY-VCH Verlag GmbH & Co. KGaA, Weinheim under Creative Commons CC BY 4.0 license. HRTEM images evidencing efficient CO_2 adsorption on single $Ti_3C_2T_x$ sheets after pretreatment steps; (j) initial preparation at RT, (k) after 700 °C in vacuum, (l) H_2 exposure at 700 °C, and (m) CO_2 exposure at 100 °C. Adapted with permission from a study by Persson et al. [11]. Copyright (2018) WILEY-VCH Verlag GmbH & Co. KGaA, Weinheim. TEM, transmission electron microscope; EELS, electron energy loss spectroscopy; HRTEM, high-resolution TEM; ED, electron diffraction.

region, so the acquisition requires less time and therefore less electron radiation dose, which may be damaging to the sample. This allows us to reduce irradiation damage for the beam-sensitive T-groups, see further discussion in the following context. However, interpretation of VEELS also requires comparison with computational efforts [87]. Fig. 10(f) shows an experimental VEELS spectrum obtained by Magne et al. [88] on the multilayer $Ti_3C_2T_2$ MXene. Based on DFT calculations, three configurations of termination sites were considered (C1, C2, and C3$_1$, see Fig. 10(g)). The simulated VEELS spectra for the C1, C3$_1$, and C2 configurations for $Ti_3C_2(T = OH)_2$ and simulated spectra for C1 and C2 configurations for $Ti_3C_2(T = F)_2$ are shown in Fig. 10(h) and (j), respectively. Theoretical spectra were compared with the experimental one in terms of appearance and shape of features A, B, C, and BP. This comparison shows that spectra calculated for T = OH are in better agreement with experiment compared with T = F. All simulated spectra for T = OH quite closely reproduce features B, C, and B.P. of experimental VEELS. However, in the region around 6 eV, where the experimental feature A is observed, the spectrum simulated for C2 configuration is flat (Fig. 10(i)). Therefore, the conclusion was that investigated MXene is predominantly terminated with OH groups in C1 and C3$_1$ configurations.

Low-loss EELS also allows to probe into local plasmonic excitations with high spatial resolution. It should be noted that to observe

such features requires high *energy* resolution and therefore demands using the monochromated EELS systems [81,87,89]. El-Demellawi et al. [81] used STEM imaging combined with ultra-high-resolution EELS to visualize transversal and longitudinal surface plasmon (SP) modes and correlate their spatial distribution with the shape, size, and thickness of $Ti_3C_2T_x$ flakes. Fig. 10(k) shows EEL spectra (with zero-loss peak subtracted) obtained from various areas of the $Ti_3C_2T_x$ flake (shown in the inset). Six distinct features were identified as dipole (0.44 eV), quadrupole (0.66 eV), first- (0.8 eV) and higher-order central (0.95 eV), transversal (1.7 eV) SP modes, and interband transition (3.5 eV). By tracing the spatial distribution of the intensity maxima of these features, EELS intensity maps corresponding to each peak were obtained (Fig. 10(l–q)). The authors also demonstrated that optical properties of MXene flake strongly relate to its morphology and additional heating experiments revealed the tunability of SP excitations by *in situ* tailoring of the surface groups.

Quantification of elements by EDX in both the SEM and (S)TEM, as well as by EELS in the (S)TEM are possible and have been used in many of the papers cited here. EELS is best used for quantification of ionization edges in the 100−1000 eV range, while EDX is best used above 1 keV and is limited upward by the accelerating voltage (in the SEM), but edges up to 40 keV are easily detected. In general, the approach is very simple for both methods, but suffer
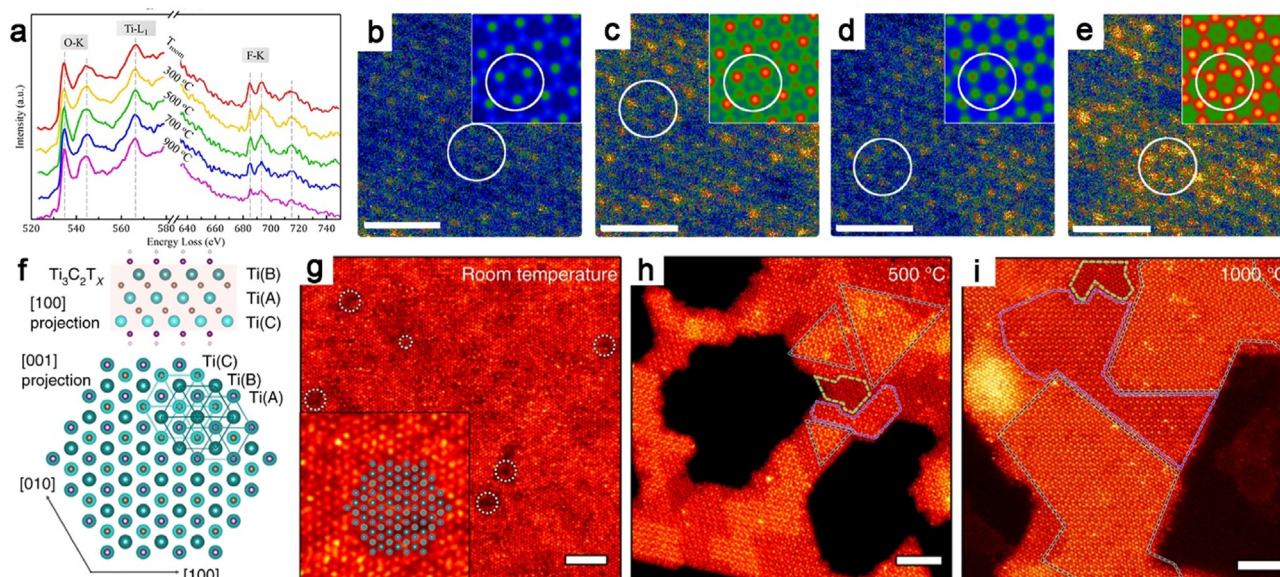
Fig. 12. In situ resistive heating and e-beam irradiation of MXenes: (a) EELS showing temperature-dependent desorption of F terminations. Adapted with permission from a study by El-Demellawi et al. [81]. Copyright (2018) American Chemical Society. (b–e) HAADF mages of a single $Ti_3C_2T_x$ sheet surface at 500 °C after preheating to 700 °C in vacuum to remove F-terminations. Insets presents HAADF simulations for (b) an unterminated surface, (c) O-terminated top surface, (d) O-terminated bottom surface, and (e) O-terminations on both surfaces. Adapted from a study by Persson et al. [75]. Copyright (2018) IOP Publishing under Creative Commons Attribution 3.0 license. (f) Atomic models of $Ti_3C_2T_x$ as seen from a study by Zhang et al. [100] and [001] directions. (g) Atomically resolved HAADF images of [001] $Ti_3C_2T_x$ at RT. Ti vacancies highlighted with white rings. (h) HAADF image after heating and e-beam irradiation at 500 °C in vacuum. Black regions correspond to pores and brighter regions to TiC adlayers. (i) HAADF image after heating at 1000 °C in vacuum. Adapted from a study by Sang et al. [83]. Copyright (2018) Springer Nature under Creative Commons CC BY license. HAADF, high-angular annular dark-field; EELS, electron energy loss spectroscopy.

from many artefacts including lack of standards and uncertain fluorescence yield. Therefore, quantification of rough elemental ratios can be readily performed, while accurate quantifications (with 1−2% error bars) require extensive control of the experimental conditions.

Owing to improved optics, the modern electron microscopes, both SEM and (S)TEM, deliver more beam current at better spatial resolution. In parallel more accommodating optics have been developed that allow for complicated devices, such as environmental chambers, to be placed inside the microscope. This further enables experiments where samples are subjected to external stimuli, while the structural or chemical changes are observed and quantified in real time. Such *in situ* and *in operando* experiments generate a more detailed understanding of materials properties in applications. Available stimuli range from mechanical indentation to biasing, resistive heating and environmental exposures to liquids and gases [90].

In situ (S)TEM is the only investigation technique that can capture dynamic processes with atomic clarity in real time and reactive environments [91]. As such it has been used already in several MXene investigations. Ghassemi et al. [92] performed the first *in situ* TEM investigation on oxidation mechanisms of $Ti_3C_2T_x$ MXene, where they used *in situ* environmental TEM (ETEM) to monitor MXene particles at the nanoscale during oxidation at different times scales and temperature regimes. It was established by TEM imaging and ED that oxidation by rapid heating result in the formation of carbon-supported anatase TiO_2 at 500 °C for 20 s, see Fig. 11(a−b), while slow heating mainly yields carbon-supported rutile TiO_2 above 260 °C for 0.5 h, Fig. 11(c−d).

Oxidation at the atomic scale and on single MXene sheets was explored by Persson et al. [93] using a new-generation resistive heating nanoreactor inside an aberration-corrected ETEM to examine single flakes of $Ti_3C_2T_x$ MXene during reaction in an O_2 environment. The structural evolution as function of temperature

was monitored by HRTEM imaging and corresponding EDPs, see Fig. 11(e−h) for surface morphologies and structural integrity analysis of $Ti_3C_2T_x$ at (e) RT, (f) 175 °C, (g) 350 °C, (h) 450 °C. Persson et al. further established that surface O coverage increased as a function of temperature up and beyond the speculated point of full coverage before a transformation into TiO_2 occurred at 450 °C, see Fig. 11(i) as identified both by ED and EELS.

MXenes were theoretically predicted as promising CO_2 adsorbers. However, as-prepared MXene is terminated with O and F, which inhibits spontaneous CO_2 adsorption. In a report by Persson et al. [11] $Ti_3C_2T_x$ MXene was investigated as an efficient adsorber for carbon capture using *in situ* ETEM. An effective strategy to rid the surface of F and O was developed employing preheating in vacuum and H_2 treatment after which CO_2 adsorption was observed, see Fig. 11(j−m). Equally important was the finding that the native surface terminations are possible to substitute using this approach, which opens up for further improving electronic and electrochemical properties.

It is challenging to acquire atomically resolved TEM images of MXenes. Surface contamination stemming from the etching, washing, and delamination process give rise to a noise level that is significantly higher than the signal of the few atomic thick layer MXene. In 2017, Persson et al. [75] demonstrated *in situ* vacuum heating as an efficient approach to remove hydrocarbon contamination (>100 °C) and delamination residuals from the preparation (>350 °C) enabling clean surfaces to be imaged. El-Demellawi et al. [81] further demonstrated efficient removal of surface terminating fluorine using EELS after *in situ* heating up to 900 °C, see Fig. 12(a). With F removed, Persson et al. [75] was able to investigate the rearrangement of the remaining O terminations to the thermodynamically preferred A-site, see the different O arrangement patterns in Fig. 12(b−e) for; (b) an un-terminated, (c) a top-terminated, (d) a bottom-terminated, and (e) a top- and bottom-terminated surface.
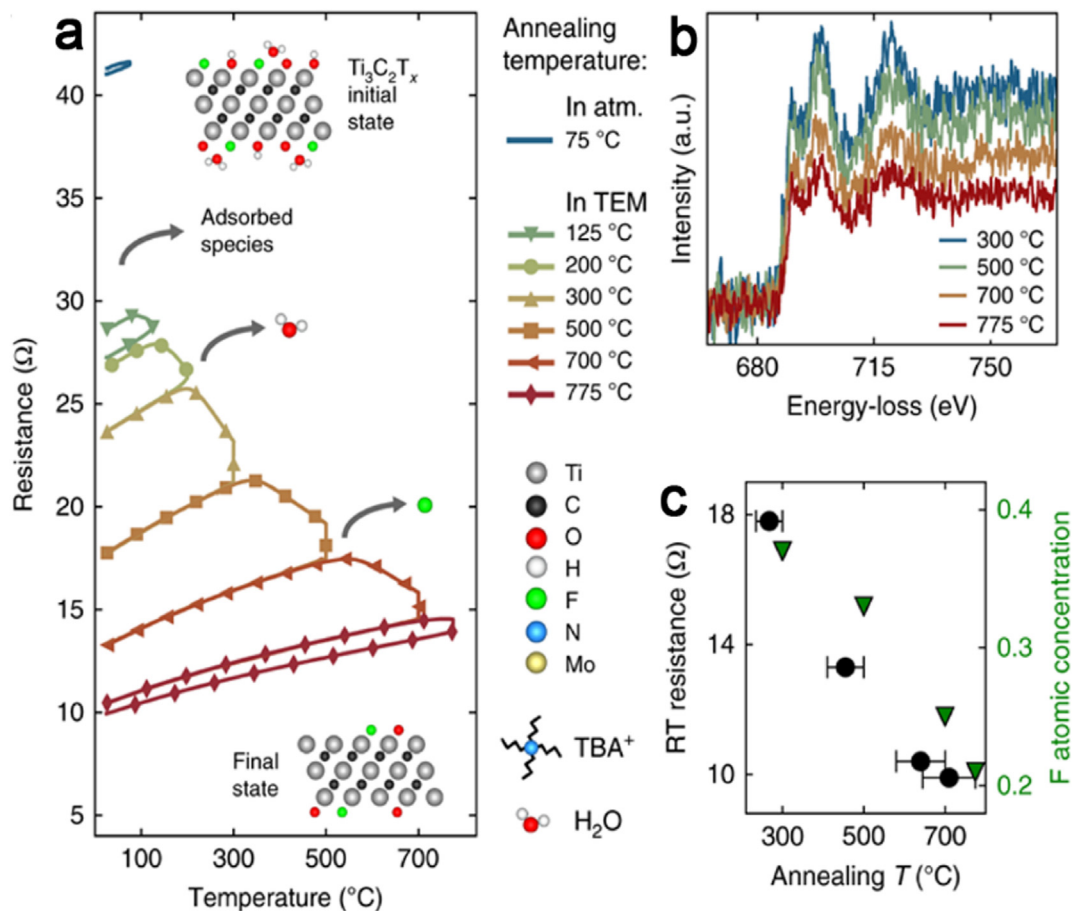
Fig. 13. In situ electric biasing of MXenes. (a) Electrical resistance as a function of temperature for $Ti_3C_2T_x$. Arrows indicate an irreversible threshold corresponding to chemical desorption from the surface. (b) EELS spectra showing F desorption with increased temperature. (c) Graph illustrating a correlation between F concentration and RT resistance as a function of temperature. Adapted from a study by Hart et al. [8]. Copyright (2019) Springer Nature under Creative Commons CC BY license. EELS, electron energy loss spectroscopy.

Another essential factor that poses as a challenge for high-resolution TEM is the electron beam damage that depends on acceleration energy and electron dose [94,95]. MXene materials are no exception and Sang et al. [83] presented how a $Ti_3C_2T_x$ MXene can undergo a phase transformation into 3D TiC growth purely driven by heating and electron beam irradiation. In Fig. 12(f), an atomic model of a [001] $Ti_3C_2T_x$ MXene surface is presented, while (g-i) shows HAADF images of; (g) an as-prepared 001 surface at RT, (h) a surface after electron beam irradiation at 500 °C, and (i) a surface after heat treatment at 1000 °C.

The correlation between structure, surface chemistry and properties is well suited for *in situ* investigations in the electron microscope, and efforts are increasing. This includes tuning of the electronic properties by either controlling transition metal combinations [96], number of M and X layers in the slab (2:1, 3:2, 4:3) [97], alloying two M element (M1, M2) [48], elemental order within layers [50,98], and lastly by different etching routines that yield various O, OH, and F ratios [8]. Hart et al. [8] investigated the effect of surface state and intercalants on the resistivity of MXenes, see Fig. 13(a). The initial decrease in resistance at 100 °C was attributed to the release of adsorbed H_2O and O_2. The second decrease starting from 200 °C was explained by the desorption of intercalated water. At 300−500 °C it was argued that partial determination causes a decrease in resistance while at 500−700 °C the removal of F terminations accounts for the final drop in resistance. Fig. 13(b) evidences the drop in F after 500 °C by EELS. In Fig. 13(c), the

correlation of F content and RT resistance after annealing to respective temperatures is presented.

The electron beam is the smallest tool to probe and tailor the structure and property of low-dimensional materials at a scale down to single atom [99]. As shown previously in Fig. 12(f−i), the electron irradiation at elevated temperatures can trigger growth of new MXene while simultaneously remove the surface terminations [83]. It should be mentioned that MXenes come as both single sheets and multilayer stacks, where irradiation of the latter was investigated by Zhang et al., who discussed a structural reorganization under the electron beam [100]. Allegedly, the M-element is displaced from the MX slabs and rearranged to fit in the space between the terminated MXene sheets, see Fig. 14(a−c).

The possibility for chemical modification by sputtering of elements from the MXene sheets was investigated by Ibragimova et al. [101], who applied a first principles approach to plan-view geometry irradiation of a $Ti_3C_2T_x$ sheet. Arguing from a perspective that MXenes are highly conductive compounds, e-beam irradiation should not affect the structure through inelastic interactions (radiolysis), elastic collisions causing sputtering of single atoms are instead more likely. The sputtering cross section, at a relevant beam current and at different accelerating voltages, was accordingly calculated for the MXene with different terminations, as shown for bottom and top MXene surfaces in Fig. 14(d−e), respectively. As is shown, the bottom (beam exit) surface species are significantly more easily sputtered while the
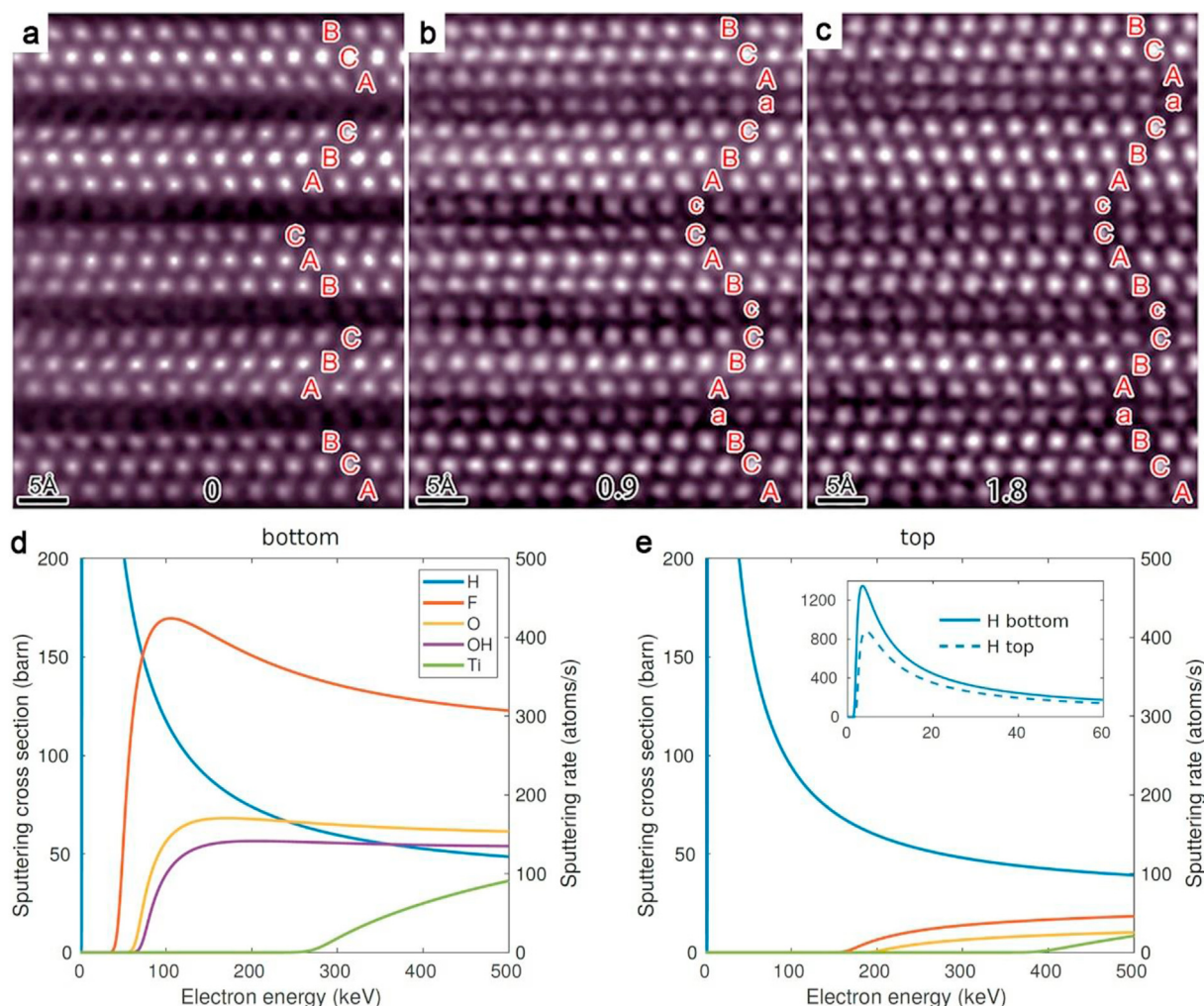
Fig. 14. Electron irradiation of MXenes (a−c) presents the STEM images of $Ti_3C_2T_x$ after irradiated for 0, 0.6, 1.2, and 1.8 ms with an electron dose rate of 1.25×10^9 $e^-/Å^2$ s at 300 kV. The originally nearly invisible T_x slabs exhibit appreciable intensities after extended exposure to the electron probe for 0.6 ms, indicating migration of Ti atoms from the Ti_3C_2 into the T_x slabs. Adapted with permission from a study by Zhang et al. [100]. Copyright (2019) American Chemical Society. (d−e) shows the calculated cross section of H, F, O, OH, and Ti and corresponding sputtering rate depending on the arriving electron energy from the bottom (d) and top (e) surface of $Ti_3C_2O_{0.5}F_{0.25}OH_{0.25}$. The inset shows the (negligible) H cross sections at low electron energies. Adapted from a study by Ibragimova et al. [101]. STEM, scanning transmission electron microscopy.

top surface is more stable. Similarly, the lighter species, i.e. the surface terminations, are easier to sputter. Low accelerating voltages are preferred for experiments, as the calculation clearly shows a sputtering onset for the surface terminations on the bottom surface between 50 and 100 keV. These findings shine light on why MXenes investigated in UHV instruments may affect particularly the surface terminations more when investigated in an HV instrument. In an HV instrument, there is continuous deposition of ambient species on exposed surfaces, while for UHV there is not. A 'protective' layer of C contamination may bury and secure the surface terminations on the MXene surface. Compare for instance results between Sang and Persson, wherein the latter maintains the terminations through the experiment, and the former observes their removal [75,83].

Being the only tool available to directly investigate the structure and chemistry of micron sized particles to the single sheet and individual atom, electron microscopes are essential in materials research and have proven invaluable in MXene research and development as shown in the present review. It is shown how electron microscopes have paved the way for new findings and contributed to the success of this new family of materials.

Herein, we have reviewed the investigation of MXenes and their parent MAX phase precursors using electron microscopy. Among many observations made throughout this review, it is clear that extensive research activities are ongoing around the world to investigate MXenes by means of electron microscopy. We have thoroughly reviewed the corresponding width of applications that are used to investigate MXenes, whether in the SEM or in the (S) TEM. With each application, we have also discussed the limitations and prospects that the users of microscopy data need to consider when evaluating results or planning experiments. We have additionally outlined *in situ* electron microscopy as an increasingly attractive tool for structural and chemical tailoring of MXenes, while observing the dynamic process in real time using structural imaging and chemical or elemental spectroscopy.

Among the fundamental challenges of electron microscopy of MXenes, but also to XPS and similar techniques, remain the identification and visualization of surface terminations. While the MXenes are typically prepared in liquid, the 2D material is typically investigated at high vacuum or even ultrahigh vacuum conditions in the microscope. These differences may cause reorganization, desorption and recombination of the terminations. Furthermore,

during preparation of MXenes, a range of inorganic and organic chemicals are used and remain on the surfaces when inserted in the microscope, and affect the interpretation of what is observed.

As was also discussed in this review is the damaging effect caused by the electron beam on the samples during investigation. While the damage can be reduced by lowering the accelerating voltage, changes at the individual atomic level will be inevitable and will therefore fundamentally limit the interpretation at some point.

Finally, we foresee that MXenes will significantly affect the future of 2D materials research. Their ability for structural and chemical tailoring is a prerequisite for unprecedented properties and applications in the years to come. It is also clear that electron microscopy will be necessary to fundamentally understand what causes these properties.

Author contribution

Hatim Alnoor: Data curation, Writing − Original draft preparation, Reviewing, **Anna Elsukova**: Data curation, Writing − Original draft preparation, Reviewing, **Justinas Palisaitis:** Data curation, Writing − Original draft preparation, Reviewing, **Ingemar Persson:** Data curation, Writing − Original draft preparation, Reviewing, **Eric Nestor Tseng:** Data curation, Writing − Original draft preparation, Reviewing, **Jun Lu**: Writing − Reviewing and Editing, **Lars Hultman:** Writing − Reviewing and Editing, and **Per O.Å. Persson:** Supervision, Writing − Original draft preparation, Reviewing and Editing

Declaration of competing interest

The authors declare that they have no known competing financial interests or personal relationships that could have appeared to influence the work reported in this paper.

Acknowledgments

References

[1] K.S. Novoselov, et al., Electric field in atomically thin carbon films, Science (80-.) 306 (5696) (Oct. 2004) 666−669, https://doi.org/10.1126/science.1102896.

[2] K. Khan, et al., Recent developments in emerging two-dimensional materials and their applications, J. Mater. Chem. C 8 (2) (Jan. 2020) 387−440, https://doi.org/10.1039/c9tc04187g.

[3] Y. Gogotsi, B. Anasori, The rise of MXenes, ACS Nano 13 (8) (Aug. 27, 2019) 8491−8494, https://doi.org/10.1021/acsnano.9b06394. American Chemical Society.

[4] M. Naguib, et al., Two-dimensional nanocrystals produced by exfoliation of Ti3AlC2, Adv. Mater 23 (37) (Oct. 2011) 4248−4253, https://doi.org/10.1002/adma.201102306.

[5] M. Ghidiu, M.R. Lukatskaya, M.Q. Zhao, Y. Gogotsi, M.W. Barsoum, "Conductive two-dimensional titanium carbide 'clay' with high volumetric capacitance, Nature 516 (7529) (Dec. 2015) 78−81, https://doi.org/10.1038/nature13970.

[6] M. Li, et al., Element replacement approach by reaction with lewis acidic molten salts to synthesize nanolaminated MAX phases and MXenes, J. Am. Chem. Soc. 141 (11) (Mar. 2019) 4730−4737, https://doi.org/10.1021/jacs.9b00574.

[7] P.O.Å. Persson, J. Rosen, Current state of the art on tailoring the MXene composition, structure, and surface chemistry, Curr. Opin. Solid State Mater. Sci. 23 (6) (Dec. 2019) 100774, https://doi.org/10.1016/j.cossms.2019.100774.

[8] J.L. Hart, et al., Control of MXenes' electronic properties through termination and intercalation, Nat. Commun. 10 (1) (Dec. 2019) 1−10, https://doi.org/10.1038/s41467-018-08169-8.

[9] M. Khazaei, et al., Novel electronic and magnetic properties of two-dimensional transition metal carbides and nitrides, Adv. Funct. Mater. 23 (17) (May 2013) 2185−2192, https://doi.org/10.1002/adfm.201202502.

[10] Y. Li, et al., A general Lewis acidic etching route for preparing MXenes with enhanced electrochemical performance in non-aqueous electrolyte, Nat. Mater. 19 (8) (Apr. 2020) 894−899, https://doi.org/10.1038/s41563-020-0657-0.

[11] I. Persson, et al., 2D transition metal carbides (MXenes) for carbon capture, Adv. Mater. 31 (2) (Jan. 2019) 1805472, https://doi.org/10.1002/adma.201805472.

[12] J. Halim, et al., X-ray photoelectron spectroscopy of select multi-layered transition metal carbides (MXenes), Appl. Surf. Sci. 362 (Jan. 2016) 406−417, https://doi.org/10.1016/j.apsusc.2015.11.089.

[13] Editorial Board, Nano Today, vol. 7, Feb. 2012, p. CO2, https://doi.org/10.1016/s1748-0132(12)00006-0.

[14] Ludwig Reimer, Scanning Electron Microscopy, Springer, Berlin, Heidelberg, 1998.

[15] B. Anasori, M.R. Lukatskaya, Y. Gogotsi, 2D metal carbides and nitrides (MXenes) for energy storage, Nat Rev Mat vol. 2 (2) (Jan. 17, 2017), https://doi.org/10.1038/natrevmats.2016.98. Nature Publishing Group.

[16] B. Anasori, A. Sarycheva, S. Buondonno, Z. Zhou, S. Yang, Y. Gogotsi, 2D metal carbides (MXenes) in fibers, Mater. Today 20 (8) (Oct. 2017) 481−482, https://doi.org/10.1016/j.mattod.2017.08.001.

[17] M.H. Tran, et al., Adding a new member to the MXene family: synthesis, structure, and electrocatalytic activity for the hydrogen evolution reaction of V4C3Tx, ACS Appl. Energy Mater. 1 (8) (Aug. 2018) 3908−3914, https://doi.org/10.1021/acsaem.8b00652.

[18] M. Naguib, et al., Two-dimensional transition metal carbides, ACS Nano 6 (2) (Feb. 2012) 1322−1331, https://doi.org/10.1021/nn204153h.

[19] B. Anasori, et al., Two-dimensional, ordered, double transition metals carbides (MXenes), ACS Nano 9 (10) (Oct. 2015) 9507−9516, https://doi.org/10.1021/acsnano.5b03591.

[20] J. Luo, et al., Pillared structure design of MXene with ultralarge interlayer spacing for high-performance lithium-ion capacitors, ACS Nano 11 (3) (Mar. 2017) 2459−2469, https://doi.org/10.1021/acsnano.6b07668.

[21] L. Xiu, Z. Wang, M. Yu, X. Wu, J. Qiu, Aggregation-resistant 3D MXene-based architecture as efficient bifunctional electrocatalyst for overall water splitting, ACS Nano 12 (8) (Aug. 2018) 8017−8028, https://doi.org/10.1021/acsnano.8b02849.

[22] D. Zhao, et al., Alkali-induced crumpling of Ti3C2Tx (MXene) to form 3D porous networks for sodium ion storage, Chem. Commun. 54 (36) (2018) 4533−4536, https://doi.org/10.1039/c8cc00649k.

[23] X. Wang, et al., 3D Ti3C2Tx aerogels with enhanced surface area for high performance supercapacitors, Nanoscale 10 (44) (Nov. 2018) 20828−20835, https://doi.org/10.1039/c8nr06014b.

[24] V. Natu, M. Clites, E. Pomerantseva, M.W. Barsoum, Mesoporous MXene powders synthesized by acid induced crumpling and their use as Na-ion battery anodes, Mater. Res. Lett 6 (4) (Apr. 2018) 230−235, https://doi.org/10.1080/21663831.2018.1434249.

[25] R. Thakur, et al., Insights into the thermal and chemical stability of multi-layered V2CTx MXene, Nanoscale 11 (22) (Jun. 2019) 10716−10726, https://doi.org/10.1039/c9nr03020d.

[26] M. Seredych, et al., High-temperature behavior and surface chemistry of carbide MXenes studied by thermal analysis, Chem. Mater. 31 (9) (May 2019) 3324−3332, https://doi.org/10.1021/acs.chemmater.9b00397.

[27] J. Liu, et al., Hydrophobic, flexible, and lightweight MXene foams for high-performance electromagnetic-interference shielding, Adv. Mater. 29 (38) (Oct. 2017), https://doi.org/10.1002/adma.201702367.

[28] M.Q. Zhao et al., Flexible MXene/carbon nanotube composite paper with high volumetric capacitance, Adv. Mater. 27 (2) (Jan. 2015) 339−345, https://doi.org/10.1002/adma.201404140.

[29] X. Xie, et al., Porous heterostructured MXene/carbon nanotube composite paper with high volumetric capacity for sodium-based energy storage devices, Nanomater. Energy 26 (Aug. 2016) 513−523, https://doi.org/10.1016/j.nanoen.2016.06.005.

[30] D.B. Williams, C.B. Carter, Transmission Electron Microscopy: A Textbook for Materials Science, Springer, Boston, MA, 2009.

[31] X.L. Ma, Y.L. Zhu, X.H. Wang, Y.C. Zhou, Microstructural characterization of bulk Ti3AlC2 ceramics, Philos. Mag. A 84 (28) (Oct. 2004) 2969−2977, https://doi.org/10.1080/14786430410001716197.

[32] T. Lapauw, et al., Synthesis of the novel Zr3AlC2 MAX phase, J. Eur. Ceram. Soc. 36 (3) (Feb. 2016) 943−947, https://doi.org/10.1016/j.jeurceramsoc.2015.10.011.

[33] L. Guo, X. Wang, Z.Y. Leong, R. Mo, L. Sun, H.Y. Yang, Ar plasma modification of 2D MXene Ti3C2Tx nanosheets for efficient capacitive desalination, FlatChem 8 (Mar. 2018) 17−24, https://doi.org/10.1016/j.flatc.2018.01.001.

[34] Y. Yao, L. Lan, X. Liu, Y. Ying, J. Ping, Spontaneous growth and regulation of noble metal nanoparticles on flexible biomimetic MXene paper for

bioelectronics, Biosens. Bioelectron. 148 (Jan. 2020) 111799, https://doi.org/10.1016/j.bios.2019.111799.

[35] Z.J. Lin, M.J. Zhuo, Y.C. Zhou, M.S. Li, J.Y. Wang, Microstructural characterization of layered ternary Ti2AlC, Acta Mater. 54 (4) (Feb. 2006) 1009–1015, https://doi.org/10.1016/j.actamat.2005.10.028.

[36] C. Peng, H. Wang, H. Yu, F. Peng, (111) TiO2-x/Ti3C2: synergy of active facets, interfacial charge transfer and Ti3+ doping for enhance photocatalytic activity, Mater. Res. Bull. 89 (May 2017) 16–25, https://doi.org/10.1016/j.materresbull.2016.12.049.

[37] R. Liu, W. Li, High-thermal-stability and high-thermal-conductivity Ti2C2Tx MXene/poly(vinyl alcohol) (PVA) composites, ACS Omega 3 (3) (2018) 2609–2617, https://doi.org/10.1021/acsomega.7b02001.

[38] L. Farber, I. Levin, M.W. Barsoum, High-resolution transmission electron microscopy study of a low-angle boundary in plastically deformed Ti3SiC2, Phil. Mag. Lett. 79 (4) (1999) 163–170, https://doi.org/10.1080/095008399177390.

[39] A. Joulain, L. Thilly, J. Rabier, Revisiting the defect structure of MAX phases: the case of Ti4AlN3, Philos. Mag. A 88 (9) (Mar. 2008) 1307–1320, https://doi.org/10.1080/14786430802126615.

[40] A. Lipatov, et al., "Electrical and elastic properties of individual single-layer Nb4C3Tx MXene flakes, Adv. Electron. Mater. 6 (4) (Apr. 2020) 1901382, https://doi.org/10.1002/aelm.201901382.

[41] O. Mashtalir, et al., Intercalation and delamination of layered carbides and carbonitrides, Nat. Commun. 4 (1) (Apr. 2013) 1–7, https://doi.org/10.1038/ncomms2664.

[42] R.B. Rakhi, B. Ahmed, M.N. Hedhili, D.H. Anjum, H.N. Alshareef, Effect of postetch annealing gas composition on the structural and electrochemical properties of Ti2CTx MXene electrodes for supercapacitor applications, Chem. Mater. 27 (15) (Jul. 2015) 5314–5323, https://doi.org/10.1021/acs.chemmater.5b01623.

[43] F. Kong, et al., Improving the electrochemical properties of MXene Ti3C2 multilayer for Li-ion batteries by vacuum calcination, Electrochim. Acta 265 (Mar. 2018) 140–150, https://doi.org/10.1016/j.electacta.2018.01.196.

[44] C. Wang, et al., Structural transitions induced by ion irradiation in V2AlC and Cr2AlC, J. Am. Ceram. Soc. 99 (5) (May 2016) 1769–1777, https://doi.org/10.1111/jace.14118.

[45] C. Wang, et al., Role of the X and n factors in ion-irradiation induced phase transformations of Mn+1AXn phases, Acta Mater. 144 (Feb. 2018) 432–446, https://doi.org/10.1016/j.actamat.2017.11.008.

[46] H. Zhang, et al., Discovery of carbon-vacancy ordering in Nb4AlC3-x under the guidance of first-principles calculations, Sci. Rep. 5 (1) (Sep. 2015) 14192, https://doi.org/10.1038/srep14192.

[47] O.L. Krivanek, et al., Atom-by-atom structural and chemical analysis by annular dark-field electron microscopy, Nature 464 (7288) (Mar. 2010) 571–574, https://doi.org/10.1038/nature08879.

[48] B. Anasori, et al., Experimental and theoretical characterization of ordered MAX phases Mo2TiAlC2 and Mo2Ti2AlC3, J. Appl. Phys. 118 (9) (Aug. 2015), 094304, https://doi.org/10.1063/1.4929640.

[49] J. Lu, A. Thore, R. Meshkian, Q. Tao, L. Hultman, J. Rosen, "Theoretical and experimental exploration of a novel in-plane chemically ordered (Cr2/3M1/3)2AlC i-MAX phase with M = Sc and y," cryst, Growth Des 17 (11) (Nov. 2017) 5704–5711, https://doi.org/10.1021/acs.cgd.7b00642.

[50] I. Persson, et al., Tailoring structure, composition, and energy storage properties of MXenes from selective etching of in-plane, chemically ordered MAX phases, Small 14 (17) (Apr. 2018) 1703676, https://doi.org/10.1002/smll.201703676.

[51] J. Thörnberg, et al., Synthesis of (V2/3Sc1/3)2AlC i-MAX phase and V2-xC MXene scrolls, Nanoscale 11 (31) (Aug. 2019) 14720–14726, https://doi.org/10.1039/c9nr02354b.

[52] Q. Tao, et al., Two-dimensional Mo1.33C MXene with divacancy ordering prepared from parent 3D laminate with in-plane chemical ordering, Nat. Commun. 8 (1) (Apr. 2017) 1–7, https://doi.org/10.1038/ncomms14949.

[53] R. Meshkian, et al., Theoretical analysis, synthesis, and characterization of 2D W1.33C (MXene) with ordered vacancies, ACS Appl. Nano Mater. 2 (10) (Oct. 2019) 6209–6219, https://doi.org/10.1021/acsanm.9b01102.

[54] J. Halim, et al., Synthesis of two-dimensional Nb1.33C (MXene) with randomly distributed vacancies by etching of the quaternary solid solution (Nb2/3Sc1/3)2AlC max phase, ACS Appl. Nano Mater. 1 (6) (Jun. 2018) 2455–2460, https://doi.org/10.1021/acsanm.8b00332.

[55] Q. Tao, et al., Atomically layered and ordered rare-earth i-MAX phases: a new class of magnetic quaternary compounds, Chem. Mater. 31 (7) (Apr. 2019) 2476–2485, https://doi.org/10.1021/acs.chemmater.8b05298.

[56] R. Hovden, H.L. Xin, D.A. Muller, Channeling of a subangstrom electron beam in a crystal mapped to two-dimensional molecular orbitals, Phys. Rev. B Condens. Matter 86 (19) (Nov. 2012) 195415, https://doi.org/10.1103/PhysRevB.86.195415.

[57] P.D. Nellist, S.J. Pennycook, Incoherent imaging using dynamically scattered coherent electrons, Ultramicroscopy 78 (1–4) (Jun. 1999) 111–124, https://doi.org/10.1016/S0304-3991(99)00017-0.

[58] A. Howie, Image contrast and localized signal selection techniques, J. Microsc. 117 (Sep. 1979) 11–23, https://doi.org/10.1111/j.1365-2818.1979.tb00228.x.

[59] E.J. Kirkland, R.F. Loane, J. Silcox, Simulation of annular dark field stem images using a modified multislice method, Ultramicroscopy 23 (1) (Jan. 1987) 77–96, https://doi.org/10.1016/0304-3991(87)90229-4.

[60] M. Chinappi, F. Cecconi, Journal of Physics: condensed Matter PAPER Protein sequencing via nanopore based devices: a nanofluidics perspective, J. Phys. Condens. Matter 30 (20) (Feb. 2018) 145302, https://doi.org/10.1088/1361-648X.

[61] J. Halim, I. Persson, P. Eklund, P.O.A. Persson, J. Rosen, Sodium hydroxide and vacuum annealing modifications of the surface terminations of a Ti3C2 (MXene) epitaxial thin film, RSC Adv. 8 (64) (Oct. 2018) 36785–36790, https://doi.org/10.1039/c8ra07270a.

[62] J. Lu, et al., Tin+1Cn MXenes with fully saturated and thermally stable Cl terminations, Nanoscale Adv. 1 (9) (Sep. 2019) 3680–3685, https://doi.org/10.1039/c9na00324j.

[63] J. Halim, et al., Transparent conductive two-dimensional titanium carbide epitaxial thin films, Chem. Mater. 26 (7) (Apr. 2014) 2374–2381, https://doi.org/10.1021/cm500641a.

[64] R. Cheng, et al., Understanding the lithium storage mechanism of Ti3C2Tx MXene, J. Phys. Chem. C 123 (2) (Jan. 2019) 1099–1109, https://doi.org/10.1021/acs.jpcc.8b10790.

[65] Z. Hemmat, et al., Tuning thermal transport through atomically thin Ti3C2Tz MXene by current annealing in vacuum, Adv. Funct. Mater. 29 (19) (May 2019) 1805693, https://doi.org/10.1002/adfm.201805693.

[66] X. Wang, X. Shen, Y. Gao, Z. Wang, R. Yu, L. Chen, Atomic-scale recognition of surface structure and intercalation mechanism of Ti3C2Tx, J. Am. Chem. Soc. 137 (7) (Feb. 2015) 2715–2721, https://doi.org/10.1021/ja512820k.

[67] S.D. Findlay, N. Shibata, H. Sawada, E. Okunishi, Y. Kondo, Y. Ikuhara, Dynamics of annular bright field imaging in scanning transmission electron microscopy, Ultramicroscopy 110 (7) (Jun. 2010) 903–923, https://doi.org/10.1016/j.ultramic.2010.04.004.

[68] L.H. Karlsson, J. Birch, J. Halim, M.W. Barsoum, P.O.Å. Persson, Atomically resolved structural and chemical investigation of single MXene sheets, Nano Lett. 15 (8) (Aug. 2015) 4955–4960, https://doi.org/10.1021/acs.nanolett.5b00737.

[69] J. Palisaitis, I. Persson, J. Halim, J. Rosen, P.O.Å. Persson, On the structural stability of MXene and the role of transition metal adatoms, Nanoscale 10 (23) (Jun. 2018) 10850–10855, https://doi.org/10.1039/c8nr01986j.

[70] D. Zhao, et al., MXene (Ti3C2) vacancy-confined single-atom catalyst for efficient functionalization of CO2, J. Am. Chem. Soc. 141 (9) (Mar. 2019) 4086–4093, https://doi.org/10.1021/jacs.8b13579.

[71] X. Sang, et al., Atomic defects in monolayer titanium carbide (Ti3C2Tx) MXene, ACS Nano 10 (10) (Oct. 2016) 9193–9200, https://doi.org/10.1021/acsnano.6b05240.

[72] L. Qin, et al., A flexible semitransparent photovoltaic supercapacitor based on water-processed MXene electrodes, J. Mater. Chem. A 8 (11) (Mar. 2020) 5467–5475, https://doi.org/10.1039/d0ta00687d.

[73] J. Zhang, et al., Single platinum atoms immobilized on an MXene as an efficient catalyst for the hydrogen evolution reaction, Nat. Catal. 1 (12) (Dec. 2018) 985–992, https://doi.org/10.1038/s41929-018-0195-1.

[74] V. Ramalingam, et al., "Heteroatom-Mediated interactions between ruthenium single atoms and an MXene support for efficient hydrogen evolution, Adv. Mater. 31 (48) (Nov. 2019) 1903841, https://doi.org/10.1002/adma.201903841.

[75] I. Persson, et al., On the organization and thermal behavior of functional groups on Ti3C2 MXene surfaces in vacuum, 2D Mater. 5 (1) (Oct. 2018), 015002, https://doi.org/10.1088/2053-1583/AA89CD.

[76] H. Fashandi, et al., Synthesis of Ti3AuC, Ti3Au2C2 and Ti3IrC2 by noble metal substitution reaction in Ti3SiC2 for high-temperature-stable Ohmic contacts to SiC, Nat. Mater. 16 (8) (Aug. 2017) 814–818, https://doi.org/10.1038/nmat4896.

[77] B. Anasori, J. Halim, J. Lu, C.A. Voigt, L. Hultman, M.W. Barsoum, Mo2TiAlC2: a new ordered layered ternary carbide, Scripta Mater. 101 (May 2015) 5–7, https://doi.org/10.1016/j.scriptamat.2014.12.024.

[80] R.F. Egerton, Electron Energy-Loss Spectroscopy in the Electron Microscope, Springer US, 2011.

[81] J.K. El-Demellawi, S. Lopatin, J. Yin, O.F. Mohammed, H.N. Alshareef, Tunable multipolar surface plasmons in 2D Ti3C2Tx MXene flakes, ACS Nano 12 (8) (Aug. 2018) 8485–8493, https://doi.org/10.1021/acsnano.8b04029.

[82] Y. Song, et al., "Rational design of porous nitrogen-doped Ti3C2 MXene as a multifunctional electrocatalyst for Li−S chemistry, Nanomater. Energy 70 (Apr. 2020) 104555, https://doi.org/10.1016/j.nanoen.2020.104555.

[83] X. Sang, et al., In situ atomistic insight into the growth mechanisms of single layer 2D transition metal carbides, Nat. Commun. 9 (1) (Dec. 2018) 1–9, https://doi.org/10.1038/s41467-018-04610-0.

[84] H. Ikeno, T. Mizoguchi, Basics and applications of ELNES calculations, Microscopy 66 (5) (Oct. 2017) 305–327, https://doi.org/10.1093/jmicro/dfx033.

[85] D. Magne, V. Mauchamp, S. Célérier, P. Chartier, T. Cabioc'h, Site-projected electronic structure of two-dimensional Ti3C2 MXene: the role of the surface functionalization groups, Phys. Chem. Chem. Phys. 18 (45) (Nov. 2016) 30946–30953, https://doi.org/10.1039/c6cp05985f.

[86] V.J. Keast, An introduction to the calculation of valence EELS: quantum mechanical methods for bulk solids, Micron 44 (1) (Jan. 01, 2013) 93–100, https://doi.org/10.1016/j.micron.2012.08.001. Pergamon.

[87] N.D. Browning, I. Arslan, R. Erni, B.W. Reed, Low-Loss EELS in the STEM, in: Scanning Transmission Electron Microscopy, Springer, New York, 2011, pp. 659–688.

[88] D. Magne, V. Mauchamp, S. Célérier, P. Chartier, T. Cabioc'h, Spectroscopic evidence in the visible-ultraviolet energy range of surface functionalization

sites in the multilayer Ti_3C_2 MXene, Phys. Rev. B Condens. Matter 91 (20) (May 2015) 201409, https://doi.org/10.1103/PhysRevB.91.201409.

[89] V. Mauchamp, et al., Enhanced and tunable surface plasmons in two-dimensional Ti_3C_2 stacks: electronic structure versus boundary effects, Phys. Rev. B Condens. Matter 89 (23) (Jun. 2014) 235428, https://doi.org/10.1103/PhysRevB.89.235428.

[90] H.H. Pérez Garza, et al., MEMS-based system for in-situ biasing and heating solutions inside the TEM, in: European Microscopy Congress 2016: Proceedings, Wiley-VCH Verlag GmbH & Co. KGaA, 2016, pp. 237−238.

[91] T.W. Hansen, J.B. Wagner, P.L. Hansen, S. Dahl, H. Topsøe, C.J.H. Jacobsen, Atomic-resolution in situ transmission electron microscopy of a promoter of a heterogeneous catalyst, Science (80-.) 294 (5546) (Nov. 2001) 1508−1510, https://doi.org/10.1126/science.1064399.

[92] H. Ghassemi, et al., In situ environmental transmission electron microscopy study of oxidation of two-dimensional Ti_3C_2 and formation of carbon-supported TiO_2, J. Mater. Chem. A 2 (35) (Sep. 2014) 14339−14343, https://doi.org/10.1039/c4ta02583k.

[93] I. Persson, et al., How much oxygen can a MXene surface take before it breaks? Adv. Funct. Mater. (Feb. 2020) 1909005, https://doi.org/10.1002/adfm.201909005.

[94] N. Jiang, J.C.H. Spence, On the dose-rate threshold of beam damage in TEM, Ultramicroscopy 113 (Feb. 2012) 77−82, https://doi.org/10.1016/j.ultramic.2011.11.016.

[95] R.F. Egerton, P. Li, M. Malac, Radiation Damage in the TEM and SEM, Micron 35 (6) (Aug. 2004) 399−409, https://doi.org/10.1016/j.micron.2004.02.003.

[96] B. Anasori, et al., Control of electronic properties of 2D carbides (MXenes) by manipulating their transition metal layers, Nanoscale Horizons 1 (3) (May 2016) 227−234, https://doi.org/10.1039/c5nh00125k.

[97] M. Naguib, R.R. Unocic, B.L. Armstrong, J. Nanda, Large-scale delamination of multi-layers transition metal carbides and carbonitrides "MXenes", Dalton Trans. 44 (20) (May 2015) 9353−9358, https://doi.org/10.1039/c5dt01247c.

[98] M. Dahlqvist, A. Petruhins, J. Lu, L. Hultman, J. Rosen, Origin of chemically ordered atomic laminates (i-MAX): expanding the elemental space by a theoretical/experimental approach, ACS Nano 12 (8) (Aug. 2018) 7761−7770, https://doi.org/10.1021/acsnano.8b01774.

[99] A.V. Krasheninnikov, F. Banhart, Engineering of nanostructured carbon materials with electron or ion beams, Nat. Mater. 6 (10) (2007) 723−733, https://doi.org/10.1038/nmat1996. Nature Publishing Group.

[100] H. Zhang, T. Hu, W. Sun, M. Hu, R. Cheng, X. Wang, Atomic repartition in MXenes by electron probes, Chem. Mater. 31 (12) (Jun. 2019) 4385−4391, https://doi.org/10.1021/acs.chemmater.9b00470.

[101] R. Ibragimova, Z.-P. Lv, H.-P. Komsa, First Principles Study of Stability of MXenes under Electron Beam, Jul. 2020 [Online]. Available: http://arxiv.org/abs/2007.04941. (Accessed 4 August 2020).